



HAL
open science

Assessment of Molybdenum and Antimony speciation in excavated rocks and soils from the Parisian basin using mineralogical and chemical analyses coupled to geochemical modelling

Maxime Brandely, Samuel Coussy, Denise Blanc-Biscarat, Rémy Gourdon

► To cite this version:

Maxime Brandely, Samuel Coussy, Denise Blanc-Biscarat, Rémy Gourdon. Assessment of Molybdenum and Antimony speciation in excavated rocks and soils from the Parisian basin using mineralogical and chemical analyses coupled to geochemical modelling. *Applied Geochemistry*, 2022, 136, pp.105129. 10.1016/j.apgeochem.2021.105129 . hal-03654568

HAL Id: hal-03654568

<https://brgm.hal.science/hal-03654568>

Submitted on 5 Jan 2024

HAL is a multi-disciplinary open access archive for the deposit and dissemination of scientific research documents, whether they are published or not. The documents may come from teaching and research institutions in France or abroad, or from public or private research centers.

L'archive ouverte pluridisciplinaire **HAL**, est destinée au dépôt et à la diffusion de documents scientifiques de niveau recherche, publiés ou non, émanant des établissements d'enseignement et de recherche français ou étrangers, des laboratoires publics ou privés.



Distributed under a Creative Commons Attribution - NonCommercial 4.0 International License

1 **TITLE**

2 Assessment of Molybdenum and Antimony speciation in excavated rocks and soils from the Parisian
3 basin using mineralogical and chemical analyses coupled to geochemical modelling

4 **AUTHOR NAMES AND AFFILIATIONS**

5 Maxime Brandely^{a,b,c} (m.brandely@brgm.fr), Samuel Coussy^{*a} (s.coussy@brgm.fr), Denise Blanc-
6 Biscarat^b (denise.blanc-biscarat@insa-lyon.fr), Rémy Gourdon^b (remy.gourdon@insa-lyon.fr)

7 *Corresponding author

8 ^a Bureau de Recherches Géologiques et Minières (BRGM), 3 av. C. Guillemin, BP 36009, 45060
9 Orléans Cedex 2, France

10 ^b Univ Lyon, INSA Lyon, DEEP, EA7429, 69621 Villeurbanne, France

11 ^c Bouygues Travaux Publics, 1 avenue Eugène Freyssinet, 78280 GUYANCOURT, France

12 **HIGHLIGHTS**

13 Mo and Sb speciation in naturally contaminated excavated materials is characterized

14 Celestite plays a key role in Mo and Sb mobility in marly limestone samples

15 Associations with sulfides are not involved in Mo and Sb release at natural pH of the soils

16 Lime treatment changes Mo speciation and increases Mo mobility in tunnel excavation muck

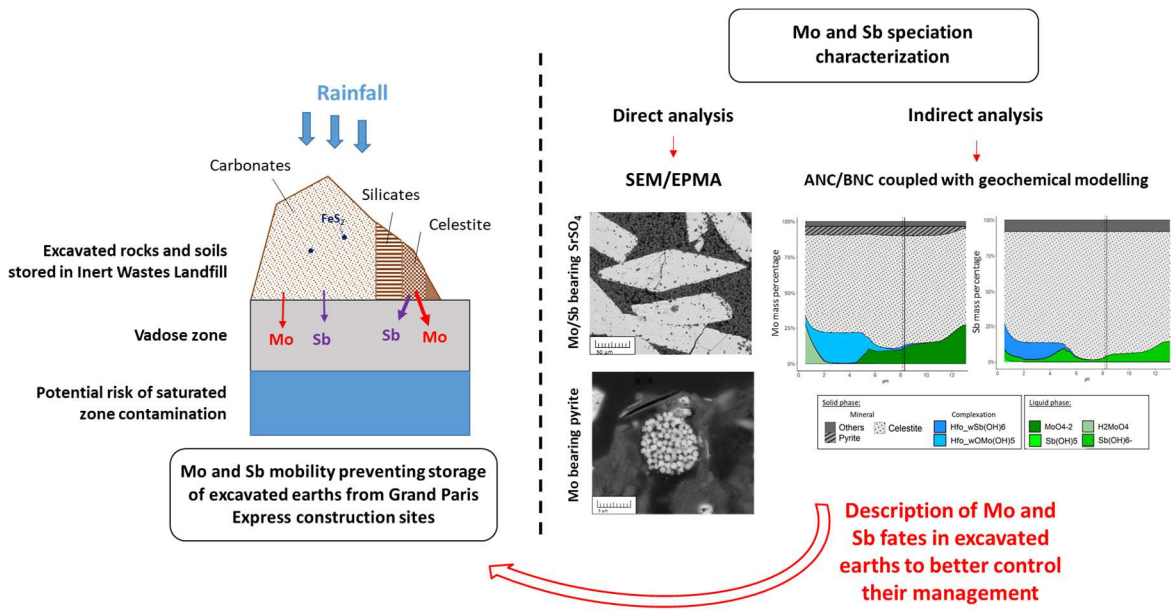
17 **KEYWORDS**

18 Molybdenum; Antimony; Excavated rocks and soils; Speciation; Geochemical Modelling

19 **ABSTRACT**

20 In the Parisian basin area, soils excavated from public works sites often reveal naturally occurring
21 trace elements contaminations, especially in Molybdenum (Mo) and Antimony (Sb). More
22 specifically, the relatively strong solubility of Mo and Sb in these excavated soils prevents them from
23 being re-used or disposed of in inert waste type landfills according to the French regulation, which is
24 based on leaching rather than total content. Furthermore, the observed total contents are in general
25 relatively low making it difficult to determine correctly the speciation of the trace elements. Yet, this
26 is a key information to estimate the potential environmental risks associated to Mo and/or Sb
27 leaching.

28 Various direct and indirect methods of mineralogical and chemical characterizations were used in
29 this study and coupled to geochemical modelling in the objective to determine the speciation and
30 potential mobility of Mo and Sb in 4 samples of excavated rocks and soils from the Parisian basin.
31 Three of them were raw materials, each one excavated in a single (but different) geological
32 formation during classic earthworks. The fourth was a tunnel muck (a slurry) dug at the border
33 between two geological formations and having undergone various treatments (e.g. liming) during the
34 process of excavation. Studied samples all showed low total content of Mo and Sb. Mobility was
35 particularly concerning for Mo in the carbonated sample (CS) and the tunnel muck (TM). Mo was
36 found systematically carried by strontium sulfates (celestite, SrSO_4) in marly limestones samples. pH
37 dependence leaching tests coupled to geochemical modelling confirmed celestite as a major sink of
38 Mo, while also pointing out its influence on Sb speciation. In the calcareous sample, Mo and Sb
39 mobility was mainly controlled by complexation onto iron oxides surfaces with high pH dependency.
40 Furthermore, in this sample, correlations between Trace Elements (TE) and Sr concentrations were
41 assumed to occur through incorporation in carbonates rather than through associations with
42 celestite. Associations with iron sulfides were suggested to be responsible for a small fraction of total
43 leachable Mo and only under basic conditions. Finally, geochemical modelling was used to describe
44 accurately Mo and Sb speciations in the tunnel muck pointing out a more complex partitioning
45 influenced by the treatment undergone during the excavation process. Results presented here
46 suggested that Mo and Sb speciations show great similarities and vary significantly depending on the
47 excavated material. It is also inferred that pH changes of materials especially expected for the
48 alkaline tunnel muck could further increase TE mobility.



51 **1. INTRODUCTION**

52 Civil engineering works (road construction, tunnel digging, etc.) generate large volumes of excavated
53 materials such as soils and rocks, which may reveal contaminations from anthropogenic or natural
54 origins. In France, infrastructure and development projects generate each year over 110 million tons
55 of excavated soils and rocks (ADEME, 2017). The Grand Paris Express Project (GPEP) is one of the
56 major public works project in Europe with creation of 200 km of mainly underground train lines and
57 almost 70 new train stations (SGP, 2019). As one of the main consequences of these works, a huge
58 amount of soils and rocks will be excavated representing a 20% increase (40 million of tons) of solid
59 waste production in the area (SGP, 2019). The bulk of these excavated soils is typically landfilled
60 because, in accordance with the Waste Framework Directive (OJEU, 2008), these soils are considered
61 as waste materials if they leave the excavation site. In this case, the demonstration of absence of
62 contamination relies on reference to the inert-waste criteria of Annex II (OJEC, 2003) of the European
63 Landfill Directive (OJEC, 1999).

64 Over the past decade, excavated soils reuse as secondary products for construction works (mainly as
65 backfills materials) has been encouraged in accordance with the objective of 70% of reuse set by the
66 European Commission (ADEME, 2017). However, although current national recommendations tend
67 to frame the recycling of excavated soils coming from uncontaminated sites, a large amount is still
68 systematically landfilled (BRGM, 2020), mainly because of the liabilities associated with their waste
69 status. One obvious problem with this approach is that the inert-waste criteria were not set for
70 natural soil materials but for waste materials (primarily construction and demolition; C&D waste).
71 This systematical landfilling is mainly related to the lack of knowledge regarding the contaminant
72 leaching behavior occurring in these soils. Indeed, historically, Trace Elements (TE) speciation studies
73 have been carried out on more acute contaminations, often originated from anthropogenic activities
74 (Halmi and Ahmad, 2014; He et al. 2012). Consequently, Molybdenum (Mo) and Antimony (Sb)
75 speciation studies in natural soil and rock materials are scarce, mainly because of the low content of
76 TE in these materials causing Detection Limit (DL) issues (Gourcy et al. 2011; Sterckeman et al.,
77 2006).

78 Overall, Mo enrichment in rocks have mainly been recorded in shales and muds, while high
79 concentrations in sandstones and carbonates are scarce (Smedley and Kinniburgh, 2017). Organic
80 Matter (OM) plays an important role in Mo speciation through indirect (complexation favored by the
81 presence of Fe-oxides associated with OM) and direct mechanisms (insertion of molybdate ions in
82 organic sulfides macromolecules through covalent bonding) (Tribovillard et al. 2004). In areas where
83 sulfate reduction occurs (*i.e.* strongly reducing conditions), Mo sulfides would form solid solutions in

84 pyrites, chalcopyrites or galena, rather than MoS_2 precipitation (Vorlicek et al. 2004 ;
85 Harkness et al., 2017 ; Smedley and Kinniburgh, 2017). Further mobilization of Mo will then be linked
86 with sulfides oxidation. In many cases, iron (Fe), aluminum (Al) and manganese (Mn) hydr-oxides are
87 also inferred to control Mo mobility through sorption/desorption mechanisms (Smedley and
88 Edmunds, 2002; Smedley et al. 2014). In such cases, water/rock interactions might cause high local
89 concentrations in surface and groundwater since oxyanions retention at oxides surfaces strongly
90 depends on pH and Eh conditions.

91 Natural Sb sources mainly come from specific environments such as hot springs, volcanic ore
92 deposits or schists (Arai, 2010). It could be found either co-precipitated and associated with metal
93 ores (pyrites, sulfosalts, oxides...) or as separate mineral ores (Roper et al. 2012; Wilson et al. 2010).
94 A huge variety of primary mineral has been acknowledged with more than 200 species mostly
95 sulfides and sulfosalts, among which stibnite (Sb_2S_3) is the main Sb ore (Wilson et al. 2010; Herath et
96 al. 2017). Dissolution of such Sb sources often lead to enrichments, which could be mitigated by (co-
97)precipitation and/or adsorption phenomena, the latter being inferred as predominant when only
98 low contamination occurs. Studies focused on Sb sorption on pure phases have shown that Mn, Al
99 and Fe (hydr-)oxides might be the more important phases controlling Sb mobility in soils
100 (Thanabalasingam and Pickering, 1990; Muller et al. 2002; Leuz et al. 2006b). As it has been seen for
101 Mo, OM interactions should not be discarded when listing Sb retention factors although mechanisms
102 are still unclear.

103 It is known that the geological characteristics of the Parisian basin often results in TE concentrations
104 above the national geological background levels, in particular for Mo and more scarcely for Sb
105 (Cabrerizo et al. 2020, Sterckeman et al., 2006). In a survey carried out in the northern Parisian basin
106 (Sterckeman et al., 2006), Sb concentrations have been shown to be globally higher than the Upper
107 Crust Continental (UCC) levels of $0.31 \text{ mg}\cdot\text{kg}^{-1}$ (Wedepohl, 1995). This enrichment was noticed in all
108 geological layers studied but was more or less important depending on the parent materials
109 composition. Hence, fluvial alluvial deposits and chalks from the later Cretaceous and Carboniferous
110 limestones were inferred to be strongly concentrated in Sb (Sterckerman et al. 2006). As far as Mo is
111 concerned, concentrations measured in sedimentary formations from the Parisian basin (Sterckeman
112 et al. 2006) did not show an overall enrichment regarding UCC or regional geological background
113 levels, which are commonly settled at $1.4 \text{ mg}\cdot\text{kg}^{-1}$ and between $0.04 \text{ mg}\cdot\text{kg}^{-1}$ and $1 \text{ mg}\cdot\text{kg}^{-1}$
114 respectively (Wedepohl, 1995; Gis Sol., 2011). However, enrichments have been noticed in particular
115 geological layers such as the fluvial alluvial deposit, chalks from the later Cretaceous and limestones
116 from the earlier Cretaceous, the Jurassic and the Carboniferous (Sterckeman et al. 2006). Mo and Sb
117 enrichments all show correlations with fine silts and Al and Fe (hydr-)oxydes inferring that sand

118 fraction and carbonate minerals might act as a diluent for TE bearing phases. Such bearing phases
119 could be mainly sulfides minerals (pyrites and chalcopyrites) for Mo (Cabrerizo et al. 2020). Finally,
120 OM is also strongly correlated with Sb enrichment in the Parisian Basin while affinities are less clear
121 in the case of Mo (Sterckeman et al. 2006; Gourcy et al. 2011). Except maybe for the topsoil layers,
122 enrichments were not linked with anthropogenic activities. They might be originated from natural
123 atmospheric fallout and/or alteration of the parent materials. In both cases, the high mobility of Mo
124 and Sb allows them to percolate from the topsoil and fix in favoring environments (presence of OM,
125 complexation at oxides surfaces...). This labile behavior is the critical parameter pointed out through
126 evacuation of excavated soils and rocks in GPEP. Other studies involving a total number of close to
127 5900 leaching tests conducted on a series of excavated soil samples from the Parisian basin
128 (unpublished) showed that Mo and Sb concentrations in the leachates were higher than the inert-
129 waste criteria in 15% and 3.5% of cases respectively. These overall results hide high disparities
130 between geological layers and are remarkable given the relatively low levels of TE total content
131 recorded.

132 This paper reports in-depth investigations on Mo and Sb speciation in four excavated materials
133 representative of TE release issues in GPEP: a calcareous soil with the highest Mo content, two marly
134 limestones with lower but still significant Mo content and tunnel excavation muck. A combination of
135 analytical tools and modelling approaches were used, which allowed to circumvent DL issues (total
136 content in Sb and Mo are below $1 \text{ mg}\cdot\text{kg}^{-1}$ and below $11 \text{ mg}\cdot\text{kg}^{-1}$ respectively). Results were exploited
137 and discussed to assess whether Mo and/or Sb mobility in these samples was controlled by particular
138 interactions with identified mineral phases. The objective was to better understand the potential
139 emissions from natural excavated soils for these TE to improve their conditions of management both
140 in terms of reuse or landfilling.

141 **2. MATERIALS AND METHODS**

142 2.1. Samples

143 Three excavated rocks were collected by Bouygues Travaux Publics Company from construction sites
144 in Paris area. The first one, hereafter referred to as calcareous sample (CS), was excavated during
145 train station earthworks in Courbevoie (Hauts-de-Seine, France) in March 2018 and was mainly
146 composed of carbonates from the Eocene period (Lutetien inferior, prof. 24 – 27 m). The two marly
147 limestone samples (MLS-A and MLS-B) were both extracted in Vitry-sur-Seine (Val-de-Marne, France)
148 in March and July 2018 respectively. MLS-A was also extracted during train station earthworks
149 corresponding to Eocene (Lutetien superior, prof. 13 – 14 m) while MLS-B was originated from a
150 deeper geological formation of the Paleocene period (Montien, prof. 14 – 23 m) and was excavated
151 during diaphragm walls construction using trench cutters and/or mechanical augers. A fourth sample
152 of tunnel muck (TM) was also studied. It was excavated by a slurry tunnel-boring machine under the
153 city of Vitry-sur-Seine and exhibited several differences compared to the three other samples. First,
154 the digging horizons were a mix between CS and MLS-A geological formations (prof. 30 – 40 m).
155 Second, its sampling followed a process including various steps directly carried out in a slurry
156 treatment plan settled in the construction site. The treatment was aimed to change slurries
157 properties making them suitable for their evacuation. Hence, mucks were firstly scalped and sand
158 fractions were removed. The residual fine fraction ($< 80 \mu\text{m}$) was limed (0.5 to 5 %wt of hydrated
159 lime) to facilitate the following step of de-watering carried out with a filter press. The treatment led
160 to the production of filtration cakes to which we will refer to as TM in the present study. Each of
161 these steps might have an impact on the mineralogical assemblage of the sample, which makes Mo
162 and Sb speciation study in TM more complicated than the simple mix between CS and MLS-A
163 geological formations might first foreshadow. All samples were stored in closed plastic bags to avoid
164 alteration due to humidity.

165 2.2. X-Ray Diffraction (XRD)

166 X-Ray Diffraction patterns were recorded in 2θ interval from 4 to 90° for each sample using a Bruker
167 D8 Advance Da Vinci diffractometer equipped with a $\text{Cu K}\alpha$ radiation tube at a scanning speed of
168 $0.03^\circ 2\theta \cdot \text{s}^{-1}$. Samples were first dried (38°C) and then micronized ($20 \mu\text{m}$) in wet media using ethanol
169 with a McCrone XRD micronizer (Retsch). The crystallized fractions were determined from their
170 powder diffractogram while their clayey fractions were estimated from oriented aggregates mounts
171 either standard, after glycolation or after a 4 h heating (490°C). Mineral identification and semi-
172 quantitative determination of relative abundances of crystalline phases was performed using the
173 software DIFFRAC.Suite. Quantitative analysis were realized with a refinement based on Rietveld

174 Method using the SIROQUANT™ V.4. software (Rietveld, 1969). It consists in describing completely
175 the pattern including the background, the shape, the position and the intensities of the observed
176 diffraction lines for the different phases with the use of structural models (Albinati and Willis, 2006).
177 Then, models parameters are refined by least squares technique until obtaining a calculated
178 diffractogram equivalent to the experimental diffractogram (Young R.A., 1993).

179 2.3. Total chemical analysis (TCA) and leaching tests

180 Major elements (Al, Ca, Fe, K, Mg, Mn, Na, P, Si and Ti) total content was analyzed by X-Ray
181 Fluorescence Spectrometry. Total trace elements concentrations in solid samples were determined
182 after calcination and a two steps mineralization by using hydrofluoric acid in presence of perchloric
183 acid followed by hydrochloric acid. The resulting solutions were analyzed by ICP-MS (THERMO X
184 Series II instrument) for TE total concentration determination (among which Mo and Sb) according to
185 the standardized procedure NF EN ISO 17294-2 (AFNOR, 2016). Finally, Total Organic Carbon (TOC)
186 was measured by dry combustion analysis according to NF ISO 10694 (AFNOR, 1995). TOC was
187 analyzed after removal of carbonates by acidification using hydrochloric acid.

188 Standardized leaching tests were carried out in triplicate according to NF EN 12457-2 (AFNOR, 2002)
189 in order to confirm TE mobility expected in our excavated materials. Samples were crushed (< 4 mm),
190 dried (38 °C) and put in contact with water at a liquid/solid (L/S) ratio of 10 for 24 h in an end-to-end
191 agitator. Supernatants were analyzed after centrifugation (30 min, 2000 g) and filtration (< 0.45 µm).
192 Eluates composition were analyzed for their concentrations in 11 trace elements (among which Mo
193 and Sb) by ICP-MS and 3 anions (Cl⁻, F⁻ and SO₄²⁻) by ionic chromatography (DIONEX). These
194 parameters were chosen as they represent 14 out of the 17 regulated ones within the European
195 Landfill Directive (OJEC, 1999).

196 2.4. Electron Probe MicroAnalysis (EPMA)

197 Polished sections of each soil sample have been prepared. They were carbon coated under secondary
198 vacuum (thickness = 20 nm) using a CRESSINGTON 308Carbon (Cressington, Watford, UK). EPMA was
199 carried out on Mo- and Sb-bearing phases pre-selected by SEM-EDS mapping. Polished sections were
200 analyzed with an electron probe microanalyser CAMECA SXFive (CAMECA, Gennevilliers, France)
201 equipped with five wavelength dispersive X-ray spectrometers (WDS) at ISTO (Orleans, France). The
202 operating conditions were accelerating voltage HV = 15 kV and beam current BC = 20 - 40 nA. Ca K α ,
203 S K α and Mo L α were measured on PET, Fe K α on LiF and Si K α , Al K α and Mg K α , on TAP. Standards
204 used for calibration were: Albite for Si, Al₂O₃ for Al, Andradite for Ca, BaSO₄ for S, Fe₂O₃ for Fe and
205 Mo metal for Mo. The phi-rho-Z method X-Phi (Merlet, 1992; 1994) was used for quantitative
206 calculation. Interferences were corrected for S (overlapping element Mo) and Mo (overlapping

207 element S). Unlike bulk spectroscopy, which might be limited by the low TE levels, this selective
208 method could be used to get quantitative measurements of Mo and Sb presence on potential
209 bearing phases selected beforehand on polished sections.. Since this study aims to investigate TE
210 speciation in excavated materials, SEM/EPMA results presented here will only be focused on the
211 identification of Mo/Sb bearing mineral phases.

212 2.5. pH dependence leaching test

213 pH dependence leaching test protocols were adapted from NF EN 14429 (AFNOR, 2015) and other
214 references (Coussy et al. 2011; Drapeau, 2018). After preliminary drying (38 °C), solid was crushed
215 (< 1mm) and a preliminary titration was performed to choose acid and basic concentrations needed
216 to cover the whole pH range. Solutions of nitric acid (HNO₃) and sodium hydroxide (NaOH) were used
217 with concentrations ranging from 0 to 1.9 mol·L⁻¹ and 0 to 0.50 mol·L⁻¹ respectively. At least 14
218 different concentrations were employed for each sample with four duplicates (or more) taken
219 randomly in the series to ensure reproducibility of the method. A L/S ratio of 10 was used and batch
220 agitation was performed with an end-to-end agitator (60 rpm, 72 h). Reaching of steady state was
221 controlled in a preliminary study where different agitation times were performed and pH
222 measurements after 72 hours did not lead to further change in pH values above 0.1 pH unit. A two
223 cases scenario was carried out to see the influence of atmospheric gas phase on samples buffer
224 capacity. In the first protocol, for MLS-A and CS, reaction bottles were regularly opened during the
225 72 h agitation ensuring renewal of gas phase whereas, in the second case (MLS-B and TM), bottles
226 were kept closed during the whole experiment. Conductivity, pH and Eh were measured after
227 solutions addition and at the end of agitation. Finally, samples were centrifuged (4500 rpm, 10 min)
228 and supernatants were filtered (0.45 µm) with syringe filters. Major elements were analyzed by
229 Inductively Coupled Plasma Optical Emission Spectrometry (ICP-OES) with a Jobin Yvon Ultima 2
230 instrument (NF EN ISO 11885; AFNOR, 2009). TE and anions concentrations were analyzed as
231 described in section 2.3. Standard deviations between duplicates were systematically below 15% for
232 Mo and Sb concentrations in the leachates.

233 2.6. Geochemical modeling

234 2.6.1. General considerations

235 The geochemical model used was supported by the PHREEQ-C software (version 3.5.0.14000;
236 Parkhurst and Appelo, 2013). Besides its ability to separate species between the gas, solid or liquid
237 phases only based on mass equation law and thermodynamic data set associated with each species,
238 the strength of PHREEQ-C comes to its adaptability to represent fairly laboratory experiments
239 (especially through the keyword REACTION). A wide range of combinations can be used to describe a

240 solid sample (mineral phases' definition, solid solutions, sorption at surface sites...) which makes it
 241 interesting for solid wastes leaching behavior modelling. Geochemical modelling was therefore used
 242 to define mineral assemblages able to represent the behavior of each sample during pH dependence
 243 leaching tests and eventually link Mo and Sb concentrations evolution with selective mineral phase
 244 dissolution.

Name	Reaction	log _k (25°C)	Kinetic control
Mineral phases identified by XRD			
Calcite	$\text{CaCO}_3 = \text{Ca}^{+2} + \text{CO}_3^{2-}$	-8.48 ^a	No
Dolomite	$\text{CaMg}(\text{CO}_3)_2 = \text{Ca}^{+2} + \text{Mg}^{+2} + 2\text{CO}_3^{2-}$	-17.13 ^a	No
Aragonite	$\text{CaCO}_3 = \text{Ca}^{+2} + \text{CO}_3^{2-}$	-8.31 ^a	No
Quartz	$\text{SiO}_2 + 2\text{H}_2\text{O} = \text{H}_4\text{SiO}_4$	3.74 ^a	Yes ^e
Gypsum	$\text{CaSO}_4 \cdot 2\text{H}_2\text{O} = \text{Ca}^{2+} + \text{SO}_4^{2-} + 2\text{H}_2\text{O}$	-4.61 ^a	No
Celestite	$\text{SrSO}_4 = \text{SO}_4^{2-} + \text{Sr}^{2+}$	-6.63 ^a	Yes ^e
Illite (Fell)	$\text{K}_{0.85}\text{Fe}_{0.25}\text{Al}_{2.35}\text{Si}_{3.4}\text{O}_{10}(\text{OH})_2 + 8.4\text{H}^+ + 1.6\text{H}_2\text{O} = 0.85\text{K}^+ + 0.25\text{Fe}^{2+} + 2.35\text{Al}^{3+} + 3.4\text{H}_4\text{SiO}_4$	9.45 ^a	Yes ^e
Palygorskite	$\text{MgAlSi}_4\text{O}_{10}(\text{OH}) + 5\text{H}^+ + 5\text{H}_2\text{O} = \text{Mg}^{2+} + \text{Al}^{3+} + 4\text{H}_4\text{SiO}_4$	37.1 ^c	Yes ^e
Sepiolite	$\text{Mg}_4\text{Si}_6\text{O}_{15}(\text{OH})_2 \cdot 6\text{H}_2\text{O} + 8\text{H}^+ + \text{H}_2\text{O} = 4\text{Mg}^{2+} + 6\text{H}_4\text{SiO}_4$	31.42 ^b	Yes ^e
Microcline	$\text{K}(\text{AlSi}_3\text{O}_8) + 4\text{H}^+ + 4\text{H}_2\text{O} = \text{Al}^{3+} + \text{K}^+ + 3\text{H}_4\text{SiO}_4$	0.05 ^a	Yes ^e
Albite	$\text{NaAlSi}_3\text{O}_8 + 4\text{H}^+ + 4\text{H}_2\text{O} = \text{Al}^{3+} + \text{Na}^+ + 3\text{H}_4\text{SiO}_4$	2.74 ^a	Yes ^e
Ettringite	$\text{Ca}_6\text{Al}_2(\text{SO}_4)_3(\text{OH})_{12} \cdot 26\text{H}_2\text{O} + 12\text{H}^+ = 2\text{Al}^{3+} + 6\text{Ca}^{+2} + 3\text{SO}_4^{-2} + 38\text{H}_2\text{O}$	56.97 ^a	No
Talc	$\text{Mg}_3\text{Si}_4\text{O}_{10}(\text{OH})_2 + 6\text{H}^+ + 4\text{H}_2\text{O} = 3\text{Mg}^{2+} + 4\text{H}_4\text{SiO}_4$	24.92 ^a	No
Mineral phases added by deduction and/or identified by SEM/EPMA analysis			
Ferrihydrite	$\text{Fe}(\text{OH})_3 + 3\text{H}^+ = \text{Fe}^{3+} + 3\text{H}_2\text{O}$	1.19 ^a	No
Goethite	$\text{FeOOH} + 3\text{H}^+ = \text{Fe}^{+3} + 2\text{H}_2\text{O}$	0.39 ^a	Yes ^e
Pyrite	$\text{FeS}_2 + 2\text{H}^+ + 2\text{e}^- = \text{Fe}^{+2} + 2\text{HS}^-$	-15.79 ^a	Yes ^e
Mineral phases allowed to precipitate			
Strontianite	$\text{SrCO}_3 = \text{HCO}_3^{2-} + \text{Sr}^{2+}$	-9.27 ^a	No
CSH0.8	$\text{Ca}_{0.8}\text{SiO}_{2.8} \cdot 1.54\text{H}_2\text{O} + 1.6\text{H}^+ = 0.8\text{Ca}^{+2} + \text{H}_4\text{SiO}_4 + 0.34\text{H}_2\text{O}$	11.05 ^a	No
Gibbsite	$\text{Al}(\text{OH})_3 + 3\text{H}^+ = \text{Al}^{+3} + 3\text{H}_2\text{O}$	7.74 ^a	No
Brucite	$\text{Mg}(\text{OH})_2 + 2\text{H}^+ = \text{Mg}^{2+} + 2\text{H}_2\text{O}$	17.1 ^a	No
Powellite	$\text{CaMoO}_4 = \text{Ca}^{+2} + \text{MoO}_4^{-2}$	-7.9 ^a	No
Ca(Sb(OH) ₆) ₂	$\text{Ca}(\text{Sb}(\text{OH})_6)_2 = \text{Ca}^{2+} + 2\text{Sb}(\text{OH})_6^-$	-12.55 ^d	No

245 *Table 1: Mineral phases used to model pH dependence leaching tests with PHREEQ-C along with their*
 246 *dissolution reactions and the associated solubility constant at 25°C. ^aGiffaut et al. (2014); ^bSinger A.*
 247 *(1977); ^cBlanc et al. (2012); ^dCornelis et al. (2012); ^eMarty et al. (2015)*

248 The geochemical modelling methodology was based on three main steps: (i) integration of the
249 mineralogical assemblages of each excavated material based on XRD and EPMA results as input data,
250 (ii) modelling of mineral assemblages and major elements behavior during pH dependence leaching
251 tests and (iii) modelling of Mo and Sb behavior. A trials and errors approach has been used and step
252 (ii) and (iii) were repeated until a satisfyingly match was found between experimental and modeling
253 results. The goodness of the fit was evaluated through visual comparison and computation of the
254 logarithm of the Root Mean Square Error ($RMSE_{\log}$) to control the proportion of experimental data
255 represented by modelling results within one order of magnitude (Dijkstra et al., 2009). The method
256 of calculus and goodness-of-fit results for geochemical models discussed in this paper are given in
257 Supplementary Information. Improvement or degradation of representation between each iteration
258 were assessed according several hypotheses. These hypotheses are described below and they were
259 mainly focused on solid phase and Mo/Sb speciation (from the initial mineral phase quantities to the
260 way of taking into account Mo/Sb-bearing phases).

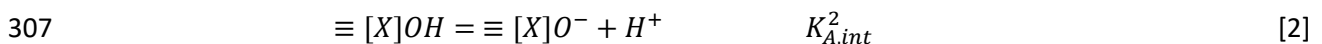
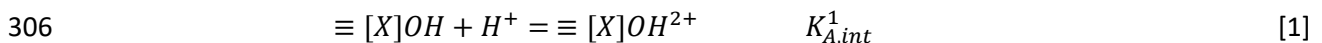
261 Initial simulations of pH dependence leaching tests were realized using quantities for each mineral
262 phase as analyzed by XRD. Comparison with experimental data of general parameters (pH, Eh and
263 conductivity) as long as major elements behavior over the pH range has led us to make adjustments
264 through adaptation of mineral phases initial quantities and/or the addition of phases likely to
265 precipitate during batch leaching tests. Table SI-1 presents mineral phases quantities used in
266 geochemical modelling for each excavated material. All thermodynamic data used for solid phase
267 modelling are summarized in Table 1. Most of them were extracted from Thermochimie v10a (Giffaut
268 et al. 2014). This thermodynamic database contains a large set of major components representative
269 of geological repository, which could be find in rocks and soils excavated from GPE construction sites.
270 Occasional lacking mineral phases were added as reported in Table 1. Thermochimie can be found in
271 a version in which activities of aqueous species are calculated through the Specific ion Interaction
272 Theory (SIT) instead of the classic Debye-Hückel equation used in Thermoddem. In this study, SIT was
273 used since it has been shown to be more suitable to represent systems with high ionic strength as
274 obtained at extreme pH during pH dependence leaching tests (Trémosa et al. 2014; Grente et al.
275 1997).

276 In a context of pH dependence leaching tests modelling, time and pH influence on mineral phase's
277 dissolution is of primary importance but often neglected. Our experimental results showed that
278 major elements were far from being totally released even at the lowest pH (except for Ca and Mg)
279 inferring incomplete dissolutions for most mineral phases. Thus, reaction rates were taken into
280 account for dissolution and precipitation of initially present mineral phases (except for carbonated
281 minerals and gypsum). Reaction rates used derived from the transition state theory (TST) for which

282 Marty et al. (2015) proposed complete kinetics parameters for a list of 15 mineral phases. All the
 283 parameters were used as computed by Marty et al. (2015) except for the mineral phase's reactive
 284 surface area (RSA) that we used as an optimization lever to describe the incomplete dissolution
 285 observed experimentally. Indeed, although values for RSA could be extracted from BET
 286 measurements for pure phases, large variation could occur for the same phase taken in a global
 287 mineral assemblage and measurement of independent RSA become difficult. Hence, by increasing or
 288 decreasing RSA (*i.e.* by accelerating or slowing dissolution rates), we attempted to represent major
 289 elements concentration maxima, which was often obtained at $\text{pH} < 2$ and could be linked to the
 290 maximum dissolution of the corresponding mineral phases).

291 2.6.2. Trace Elements modelling

292 Mo and Sb were uploaded in the geochemical model in two different ways: (i) exchangeable and (ii)
 293 in association with a mineral phase. The exchangeable fraction was established from standardized
 294 leaching test results and surface complexation models. Although several iron phases might coexist in
 295 mineral assemblages, no direct assessments were made to decipher the major oxide types in our
 296 samples. Hence, TE complexation at iron (hydr-)oxides surfaces was taken into account considering a
 297 generic reactive iron (hydr-)oxides whose behavior has been linked to goethite (FeOOH), given the
 298 fact that different iron (hydr-)oxides occurring in soils might react in a similar way. Thus, total moles
 299 of surface sites varied according to precipitation and/ or dissolution of goethite, which is convenient
 300 to qualitatively represent complexation at acidic pH where iron (hydr-)oxides are expected to (at
 301 least partially) dissolve. Iron (hydr-)oxides were introduced in the model through a goethite initial
 302 quantity settled at 25 %wt of total Fe in each sample. Surface reactive sites were defined according
 303 to the Generalized Two Layer Model (GTLM) (Dzombak and Morel, 1990). Such approach needs
 304 available data for protonation and deprotonation of each type of surfaces as given by Equations [1]
 305 and [2].



308 where $\equiv [X]OH$, $\equiv [X]O^-$ and $\equiv [X]OH^{2+}$ represent neutral, negatively and positively charged
 309 surfaces respectively; $[X]$ represents Fe atoms, $K_{A,int}^1$ and $K_{A,int}^2$ represent the intrinsic acidity
 310 constant of protonation and deprotonation respectively.

311 Proportions of available strong and weak surface sites were fixed at 0.005 and 0.2 mol per mol of
 312 reactive iron (hydr-)oxides respectively and specific surface area at $600 \text{ m}^2 \cdot \text{g}^{-1}$ (Dzombak and Morel,
 313 1990). Thermodynamic data for complexation reactions with reactive iron (hydr-)oxides were

314 implemented from Dzombak and Morel (1990). Updated values were used for Mo complexation
315 according to Gustafsson (2003) recommendations, which have shown a good ability to describe
316 sorption impact on Mo speciation at pH < 7 (Dijkstra et al. 2009). Moreover, Sb complexation data
317 has been used as optimized by Cornelis et al. (2012). All complexations reactions and their
318 corresponding solubility constants used in our model are summarized in Table 2.

	Associated reactions	log_k
Hfo_s	Protonation / Deprotonation reactions	
	$\equiv Hfo_sOH + H^+ = \equiv Hfo_sOH_2^+$	7.00 ^a
	$\equiv Hfo_sOH = \equiv Hfo_sO^- + H^+$	-8.93 ^a
	Complexation reactions	
	$\equiv Hfo_sOH + Ca^{2+} = \equiv Hfo_sOHCa^{2+}$	4.97 ^a
	$\equiv Hfo_sOH + Sr^{2+} = \equiv Hfo_sOHSr^{2+}$	5.01 ^a
	$\equiv Hfo_sOH + SO_4^{2-} + H^+ = \equiv Hfo_sSO_4^- + H_2O$	7.78 ^a
	$\equiv Hfo_sOH + SO_4^{2-} = \equiv Hfo_sOHSO_4^{2-}$	0.79 ^a
	$\equiv Hfo_sOH + MoO_4^{2-} + 2H^+ + H_2O = \equiv Hfo_sOMo(OH)_5$	17.98 ^b
	$\equiv Hfo_sOH + MoO_4^{2-} = \equiv Hfo_sOHMoO_4^{2-}$	3.14 ^b
$\equiv Hfo_sOH + Sb(OH)_6^- + H^+ = \equiv Hfo_sOSb(OH)_4 + 2H_2O$	10 ^c	
Hfo_w	Protonation / Deprotonation reactions	
	$\equiv Hfo_wOH + H^+ = \equiv Hfo_wOH_2^+$	7.29 ^a
	$\equiv Hfo_wOH = \equiv Hfo_wO^- + H^+$	-8.93 ^a
	Complexation reactions	
	$\equiv Hfo_wOH + Ca^{2+} = \equiv Hfo_wOCa^+ + H^+$	-5.85 ^a
	$\equiv Hfo_wOH + Mg^{2+} = \equiv Hfo_wOMg^+ + H^+$	-4.6 ^a
	$\equiv Hfo_wOH + Sr^{2+} = \equiv Hfo_wOSr^+ + H^+$	-6.58 ^a
	$\equiv Hfo_wOH + Sr^{2+} + H_2O = \equiv Hfo_wOSrOH + 2H^+$	-17.6 ^a
	$\equiv Hfo_wOH + SO_4^{2-} + H^+ = \equiv Hfo_wSO_4^- + H_2O$	7.78 ^a
	$\equiv Hfo_wOH + SO_4^{2-} = \equiv Hfo_wOHSO_4^{2-}$	0.79 ^a
	$\equiv Hfo_wOH + MoO_4^{2-} + 2H^+ + H_2O = \equiv Hfo_wOMo(OH)_5$	17.98 ^b
	$\equiv Hfo_wOH + MoO_4^{2-} = \equiv Hfo_wOHMoO_4^{2-}$	3.14 ^b
	$\equiv Hfo_wOH + Sb(OH)_6^- + H^+ = \equiv Hfo_wOSb(OH)_4 + 2H_2O$	13.2 ^c
$\equiv Hfo_wOH + CO_3^{2-} + H^+ = \equiv Hfo_wCO_3^- + H_2O$	12.56 ^d	
$\equiv Hfo_wOH + CO_3^{2-} + 2H^+ = \equiv Hfo_wHCO_3 + H_2O$	20.62 ^d	

319 Table 2: Protonation/Deprotonation and complexation reactions with corresponding log(k) used in
320 sorption calculations at reactive iron (hydr-)oxides surfaces (Hfo_s and Hfo_w). ^a Dzombak and Morel
321 (1990); ^b Gustafsson (2003); ^c Cornelis et al. (2012); ^d Van Geen et al. (1994)

322 As it will be discussed in section 3, Mo and Sb were considered in association with several bearing
323 phases (namely celestite, pyrite, dolomite and ettringite). Mo and Sb were directly introduced in the
324 bearing mineral phases definition with unchanged solubility constants. Although quite simplistic,
325 such an approach has the ability to represent covariations between TE and major elements
326 concentrations resulting from mineral phase's dissolution based on a possible inclusion mechanism.
327 Table 3 sums up the quantity of each element incorporated in pyrite, celestite, dolomite and/or
328 ettringite to obtain the best description of experimental results. The remaining quantity of Mo and
329 Sb could be calculated from the difference between total amount of TE (total content analysis) and
330 the quantity of TE considered in the geochemical model. This quantity represents the non-leachable
331 fraction of Mo in pH dependence leaching tests conditions, which might be partly (but not only)
332 attributable to associations with silicate minerals.

Mineral	Element	MLS-A	MLS-B	CS	TM
Celestite	Mo (mg·g ⁻¹)	0.08	0.08	-	0.06
	Sb (mg·g ⁻¹)	0.007	0.005	-	0.004
	Sr (mg·g ⁻¹)	477	477	-	477
Dolomite	Mo (mg·g ⁻¹)	-	-	0.06	0.06
	Sb (mg·g ⁻¹)	-	-	0.002	0.002
	Sr (mg·g ⁻¹)	-	-	14.1	14.1
Ettringite	Mo (mg·g ⁻¹)	-	-	-	0.008
	Sb (mg·g ⁻¹)	-	-	-	0.001
Pyrite	Mo (mg·g ⁻¹)	8.0	8.0	8.0	8.0

333 *Table 3: Mass of Mo, Sb and Sr introduced in celestite for MLS-A, MLS-B and TM, in dolomite for CS*
334 *and TM, in ettringite for TM and in pyrite for all samples. Results are given in milligrams of element*
335 *per gram of mineral phase.*

336

337 **3. RESULTS AND DISCUSSION**

338 3.1. Samples characterization

339 3.1.1. Excavated soil characteristics

	MLS-A	MLS-B	CS	TM
Major elements atomic percentage				
Al	1.02 %	0.97 %	0.41 %	1.50 %
Ca	17.16 %	19.16 %	33.02 %	36.70 %
Fe	0.71 %	0.55 %	0.38 %	< 1.00 %
K	0.31 %	0.21 %	0.11 %	0.61 %
Mg	7.56 %	8.64 %	1.03 %	7.10 %
Sr	4.06 %	0.56 %	0.16 %	0.97 %
Na	0.54 %	0.59 %	< 0.15 %	< 0.50 %
P	0.03 %	< 0.02 %	< 0.02 %	0.01 %
Si	7.39 %	7.11 %	4.33 %	6.60 %
Ti	0.10 %	0.07 %	0.04 %	0.06 %
TOC	0.34 %	< 0.1 %	0.36 %	0.63 %
Total Content (mg·kg⁻¹)				
Mo	7.2	2	10.9	4.8
Sb	0.6	<0.5	0.4	<0.5
Se	1.4	<0.5	2.76	1.2

340 *Table 4: Total content results in CS, MLS-A, MLS-B and TM for major and trace elements expressed in*
 341 *mass percentage and mg·kg⁻¹ of material respectively*

342 TCA results are shown in Table 4. As expected, calcium (Ca) was the predominant element in all
 343 samples with 36.7 %wt, 33.0 %wt, 17.2 %wt and 19.2 %wt for TM, CS, MLS-A and MLS-B respectively.
 344 For CS, all other elements (except for silicon, Si) were close or below 1 %wt suggesting a mineral
 345 assemblage almost exclusively composed of calcium carbonates which was in agreement with XRD
 346 results (Table 5). Although carbonates were also dominant in MLS-A and MLS-B, two main
 347 differences have been outlined compared to CS. First, a lower content of carbonated minerals has
 348 been identified by XRD with 70 wt% and 73 wt% respectively, with, for both samples, dolomite
 349 (CaMg(CO₃)₂) as the dominant mineral consistently with the high magnesium (Mg) content observed
 350 in TCA. Second, a higher content of sulfate bearing minerals (gypsum, CaSO₄:2H₂O and especially
 351 celestite, SrSO₄) was shown in MLS-A and MLS-B compared to CS as long as a non-negligible
 352 Strontium (Sr) concentration in these samples. Celestite content was higher in MLS-A (8 %wt) than in
 353 MLS-B (1 %wt) and, as a balance, the proportion of silicate minerals (illite, sepiolite, plagioclase and
 354 feldspath) in MLS-B was higher (20 wt% versus 14 wt% in MLS-A). XRD and TCA confirmed that TM
 355 shared characteristics with CS and MLS-A. As such, carbonated minerals were the most represented
 356 (86 %wt) almost equally split between calcite and dolomite. The slightly higher Ca content could be a

357 consequence of lime addition in the slurry treatment plan before sampling. TM also showed a non-
 358 negligible amount of celestite (i.e. 3%). Finally, lime addition might have contributed to mineral
 359 phases precipitation such as ettringite ($\text{Ca}_6\text{Al}_2(\text{SO}_4)_3(\text{OH})_{12} \cdot 26\text{H}_2\text{O}$), which was not identified in CS or
 360 MLS-A. The pH increase following lime addition probably resulted in partial dissolution of silicate and
 361 sulfate minerals forming ideal conditions to ettringite precipitation by reaction with soluble Ca
 362 (Buttress et al. 2013).

	MLS-A	MLS-B	CS	TM
Calcite	9 ± 3 %	12 ± 2 %	82 ± 3 %	47 ± 2 %
Dolomite	61 ± 3 %	61 ± 5 %	4 ± 3 %	36 ± 2 %
Celestite	8 ± 3 %	1.0 ± 0.5 %	-	3 ± 2 %
Quartz	7 ± 3 %	4 ± 1 %	4 ± 3 %	3 ± 2 %
Sepiolite	6 ± 5 %	8 ± 2 %	-	tr
Palygorskite	4 ± 5 %	4 ± 1 %	2 ± 5 %	1 ± 3 %
Illite	4 ± 5 %	5 ± 1 %	tr	3 ± 3 %
Gypsum	1 ± 3 %	2 ± 1 %	2 ± 3 %	1.5 ± 2 %
Smectite	tr	-	tr	tr
Chlorite	tr	-	tr	tr
Plagioclase	-	2 ± 1 %	1 ± 3 %	-
Feldspath	-	1.0 ± 0.5 %	-	1 ± 2 %
Aragonite	-	-	5 ± 3 %	3 ± 2 %
Amphibole	-	-	1 ± 3 %	-
Kaolinite	-	-	tr	tr
Ettringite	-	-	-	1.5 ± 2 %
Talc	-	-	-	tr

363 *Table 5: XRD results for CS, MLS-A, MLS-B and TM expressed in weight percentage of the total mineral*
 364 *assemblage. Hyphen marks are used for phases not identified while "tr" abbreviation is used when*
 365 *the phase was suggested to occur only in trace amounts.*

366 Total Organic Carbon concentrations were low in all samples attesting a relative absence of organic
 367 matter in these geological formations. Furthermore, generic parameters for anion sorption onto
 368 humic and fulvic acids are still scarce (Milne et al. 2010) and reactive organic matter groups (mostly
 369 negatively charged) might not react extensively with anions. Hence, OM influence on Mo and Sb
 370 speciation has been neglected in the present study. It was confirmed that only low levels of TE
 371 concentrations occur. The highest concentrations for Mo and Sb were noticed in CS and MLS-A with
 372 10.9 and 0.6 mg·kg⁻¹ respectively. Total Mo content of 4.8 mg·kg⁻¹ in TM was lower than both CS and
 373 MLS-A values, which was not consistent with the mix of CS and MLS-A geological formation
 374 represented in TM. This lower value might outline that a non-negligible Mo content was extracted
 375 during the slurry treatment process and more precisely during water recover after mucks pressing.
 376 High pH values induced by liming created conditions favorable to both oxyanions leaching and

377 potential bearing phase dissolution, thereby explaining such Mo impoverishment in TM. Finally, Sb
 378 was shown under the DL of $0.5 \text{ mg}\cdot\text{kg}^{-1}$ in MLS-B and TM.

379 Considering uncertainties of 2 to 3 %wt in XRD results, a good consistency between XRD and TCA was
 380 observed for Aluminum (Al), Ca, Mg, Potassium (K) and Si. Sr was also well retrieved as a celestite
 381 tracer for the two marly limestone samples and TM. Iron (Fe) was the only element for which XRD
 382 results led to underestimation of its total content in every samples. Such a result is not surprising
 383 since Fe is expected to be present mainly as iron oxy-(hydroxides), which could be ignored by XRD
 384 measurements given their poorly crystalized structures.

	DL	MLS-A	MLS-B	CS	TM
F ($\text{mg}\cdot\text{kg}^{-1}$ of DM)	1	10.7 ± 0.6	25 ± 2	9.0 ± 0.1	22 ± 1
Mo ($\text{mg}\cdot\text{kg}^{-1}$ of DM)	0.001	0.66 ± 0.07	0.30 ± 0.03	3.6 ± 0.1	3.8 ± 0.1
Sb ($\text{mg}\cdot\text{kg}^{-1}$ of DM)	0.001	0.006 ± 0.001	0.006 ± 0.001	0.009 ± 0.001	< 0.001
Se ($\text{mg}\cdot\text{kg}^{-1}$ of DM)	0.001	0.08 ± 0.01	0.030 ± 0.008	0.102 ± 0.002	0.011 ± 0.001
pH	-	7.8 ± 0.2	8.8 ± 0.1	8.8 ± 0.1	12.2 ± 0.1

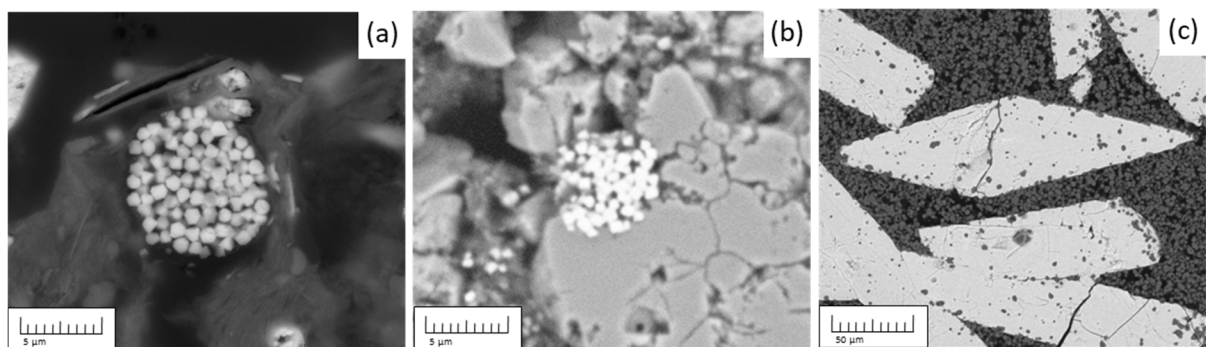
385 *Table 6: Leachates pH and concentrations obtained according to leaching tests at a L/S ratio of 10 (NF*
 386 *EN 12457-2). Values were calculated as the mean result obtained with triplicates while uncertainties*
 387 *are the corresponding standard deviation.*

388 Molybdenum mobility was confirmed by the standardized leaching test NF 12457-2 results (Table 6).
 389 Mo release was above acceptation criteria in Inert Wastes Landfills (*i.e.* $0.5 \text{ mg}\cdot\text{kg}^{-1}$ of Dry Matter
 390 (DM)) for TM, CS and MLS-A. As far as the untreated excavated earths are concerned, the overrun
 391 was more important in the case of CS with $3.6 \pm 0.1 \text{ mg}\cdot\text{kg}^{-1}$ of DM against $0.66 \pm 0.07 \text{ mg}\cdot\text{kg}^{-1}$ of DM
 392 for MLS-A. Concentrations of Mo leached in TM were even higher (*i.e.* $3.8 \pm 0.1 \text{ mg}\cdot\text{kg}^{-1}$ of DM) and
 393 represented 80 %wt of total Mo in the sample. Mo leaching in MLS-B was not concerning but, for this
 394 sample as long as in TM, it was noticed that fluorides leaching concentrations were above
 395 acceptance criteria in inert-waste landfill (*i.e.* $10 \text{ mg}\cdot\text{kg}^{-1}$ of DM) with values of 25 ± 2 and
 396 $22 \pm 1 \text{ mg}\cdot\text{kg}^{-1}$ of DM respectively. Even though no particular mobility for Sb was shown in our
 397 sample, the close behavior expected for this element compared to Mo will help us to consolidate our
 398 observations.

399 3.1.2. Mo and Sb bearing phases

400 Given the similarities between all samples regarding their major mineral phases, only CS and MLS-A
 401 were investigated by SEM/EPMA assuming that main information could be obtained through these
 402 two samples. Associations between Sb and particular mineral phases were not detected because of
 403 the low total content of Sb occurring in all samples. Pyrite, although undetected by XRD, was shown

404 to be a systematic bearing phase for Mo in samples CS and MLS-A with Mo mass percentages
405 (calculated as the mean value of seven measurements for each sample) equal to 0.8 ± 0.2 wt% and
406 1.0 ± 0.2 wt% respectively (Figure 1a and b). Such associations are direct consequences of Mo
407 chalcophile behavior and probably consist in solid solutions Mo-Fe-S. (Smedley and Kinniburgh, 2017;
408 Harkness et al. 2017). However, samples overall observations showed that the number of pyrite
409 grains remained low so that Mo-FeS₂ associated might only represent a small fraction of total Mo.
410 Unlike CS, MLS-A has shown other bearing phases for Mo. Indeed, 14 different measurements were
411 performed on celestites spread all over the polished section (Figure 1c). Mo was systematically
412 identified associated with those minerals with a mass percentage of 0.16 ± 0.08 wt%. These
413 observations have been used to feed the geochemical modeling of pH dependence leaching tests.



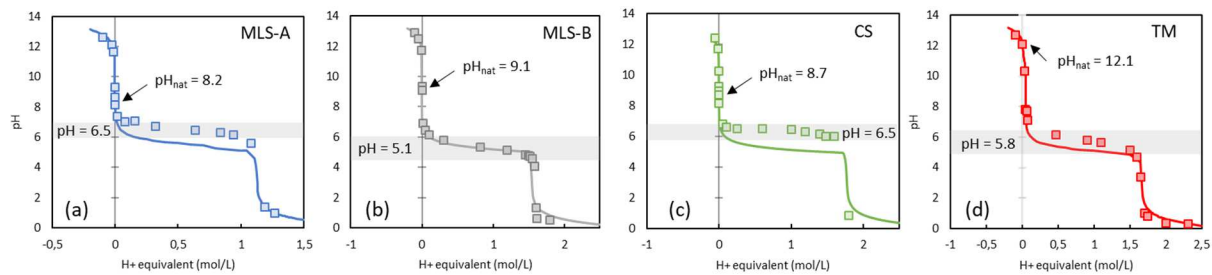
414 *Figure 1: SEM images of Mo bearing pyrites in MLS-A (a) and CS (b) as long as Mo bearing celestites*
415 *in MLS-A (c)*

416 3.2. Geochemical modelling

417 3.2.1. General description

418 As a preliminary stage, models reliability was estimated based on pH evolutions as a function of the
419 quantity of acid or base added. First, a natural batch pH (pH_0) has been determined for each sample,
420 which corresponds to batches in which solids were in contact with water only. Measurements made
421 after 72 h of agitation were 8.2, 9.1, 8.7 and 12.1 for MLS-A, MLS-B, CS and TM respectively. The
422 alkaline nature of the untreated soils was already acknowledged through pH measurement during
423 standardized leaching tests (Table 1). In the case of TM, pH value above 12 was the consequence of
424 lime addition. Modeled values were close to experimental results with a maximum difference of 0.2
425 pH units, which could be explained by the low buffer capacity from pH_0 observed in all samples.
426 Figure 2 shows experimental pH curves along with modeling results. A maximum acid neutralization
427 capacity was observed at pH of 6.3, 5.1, 6.5 and 5.8 for MLS-A, MLS-B, CS and TM respectively, which
428 was expected given the predominance of carbonates in all mineral phase's assemblages. Moreover,
429 buffer plateau lengths for each sample, which represent the quantity of protons (H^+) needed to

430 dissolve carbonate phases, were consistent with relative carbonates quantities determined by XRD
 431 and TCA. As such, CS have shown the most extended acid neutralization capacity (*ca.* 1.7 moles of
 432 $H^+ \cdot L^{-1}$) followed by TM (*ca.* 1.6 moles of $H^+ \cdot L^{-1}$), MLS-B (*ca.* 1.5 moles of $H^+ \cdot L^{-1}$) and MLS-A (*ca.* 1.0
 433 moles of $H^+ \cdot L^{-1}$). Finally, one can note that CS and MLS-A showed higher experimental pH buffer
 434 values due to renewal of atmospheric gas phase as bottles were regularly opened during agitation.



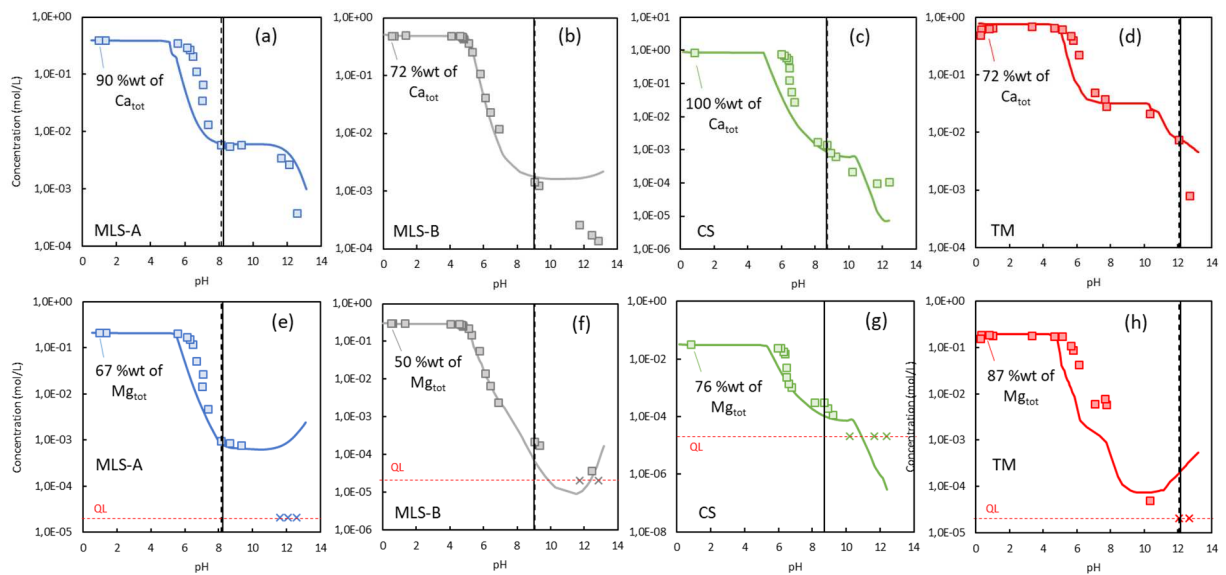
435 *Figure 2: pH dependency curves for MLS-A (a), MLS-B (b), CS (c) and TM (d) as obtained during pH*
 436 *dependence leaching tests. Solid curves and marks represent modeled and experimental data*
 437 *respectively. Negative and positive values on the X-axis of pH dependency curves are defined for basic*
 438 *and acid batches respectively. Gray areas represent the carbonates buffer area with the retained value*
 439 *explicitly written in caption. Natural batch pH are also explicitly stated and represented by an empty*
 440 *mark.*

441 3.2.2. Major elements

442 Beside the description of general parameters such as pH, major elements leaching concentrations
 443 during pH dependence leaching tests were used as tracers of mineral dissolution and/or
 444 precipitation. In the following sections, comparison between experimental and modelling results will
 445 be presented with particular attention paid on mineral phases susceptible to play a role in Mo and Sb
 446 speciation. For K and Si, results are presented in Supplementary Information.

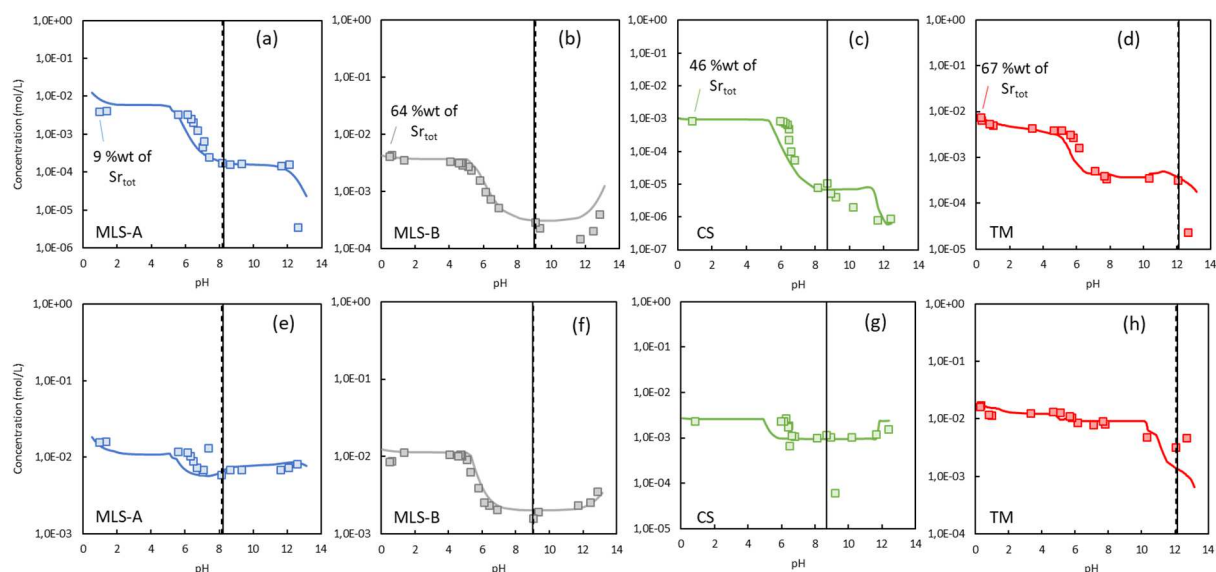
447 3.2.2.1. Calcium and Magnesium

448 The modelled and experimental concentrations during pH dependence leaching tests for MLS-A,
 449 MLS-B, CS and TM are presented in Figure 3. In each sample, decrease of pH following addition of
 450 acid solutions have resulted in a rise of Ca and Mg concentrations until complete dissolution of
 451 carbonate minerals. In TM, a shift was observed between experimental and modelling results for Ca
 452 and Mg concentrations increase during carbonates dissolution. This could be a consequence of
 453 liming, which might trigger the precipitation of more soluble polymorph of calcite (aragonite,
 454 vaterite, hydrated calcite), either through the presence of impurities (Boynton, 1980) or through
 455 carbonation of C-S-H and/or ettringite (Auroy et al., 2018). Finally, in TM, Ca concentrations increase
 456 with the very first acid addition (pH = 10.4) was linked to ettringite dissolution.



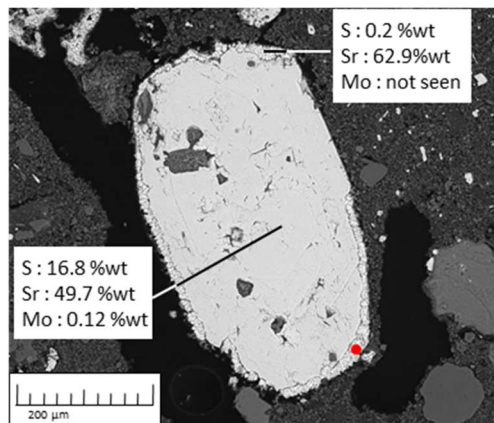
459 *Figure 3: Experimental and modelling results of Ca and Mg concentrations as a function of pH during*
 460 *pH dependence leaching tests for MLS-A (a and e), MLS-B (b and f), CS (c and g) and TM (d and h).*
 461 *Marks and solid lines represent experimental and modelling data respectively, while cross marks*
 462 *represent value below the QL. Vertical dashed and solid lines represent the experimental and*
 463 *modelled natural batch pH respectively.*

464 At pH values above pH_0 (i.e. after NaOH addition), Ca and Mg concentrations measured in each
 465 sample were found to decrease. For Ca in MLS-A (Figure 3a), concentrations diminution was only
 466 observed at $pH > 11$ and a good fit was obtained by letting ettringite precipitate (Meima and
 467 Comans, 1998). In these sulfate-rich samples, the close behavior of Mg (Figure 3e) might be
 468 explained by the potential precipitation of a hydrotalcite-like (HT) mineral (Dou et al., 2017).
 469 Regarding TM, Ca concentrations decreased above pH_0 , which was explained by further precipitation
 470 of ettringite and hydrated silicate calcium (C-S-H). For MLS-B and CS (Figure 3b and c), the drop in Ca
 471 concentration was seen immediately after the first addition of base and could not be represented by
 472 ettringite precipitation, which was consistent with the much lower sulfates content compared
 473 to MLS-A. At $pH > 11$, Mg concentrations in MLS-B were reasonably well represented by dolomite
 474 equilibrium (Figure 3f). For CS, Mg concentrations below the Quantification Limit (QL) suggested the
 475 precipitation of at least one Mg bearing phase (Figure 3g). Brucite ($Mg(OH)_2$) was the only
 476 supersaturated mineral phase able to improve Mg concentration description without interfering with
 477 the rest of the system. Mg behavior at $pH > 10$ was already linked to brucite solubility in different
 478 context such as coal fly ash (Garavaglia and Caramuscio, 1994) or Municipal Solid Wastes incinerator
 479 residues (Dijkstra et al. 2006).



481 *Figure 4: Experimental and modelling results of Sr and SO₄ concentrations as a function of pH during*
 482 *pH dependence leaching tests for MLS-A (a and e), MLS-B (b and f), CS (c and g) and TM (d and h).*
 483 *Marks and solid lines represent experimental and modelling data respectively. Vertical dashed and*
 484 *solid lines represent the experimental and modelled natural batch pH respectively*

485 Figure 4 (a, b and d) show the good fit obtained between experimental and modelling data for Sr
 486 concentration as a function of pH in MLS-A, MLS-B and TM respectively. Legitimately considered as
 487 an exclusive tracer of celestite behavior, maximum Sr concentrations at pH < 2 gave us the
 488 proportion of actually dissolved celestite, which was approximately 9 %wt, 63 %wt and 67 %wt for
 489 MLS-A, MLS-B and TM respectively. The same RSA of 0.04 m²·g⁻¹ was fixed to represent the behavior
 490 of the natural celestite occurring in both marly limestone samples while a slightly lower value of 0.01
 491 m²·g⁻¹ was used for TM (Table SI-1). On the other side of the pH range, at pH values above 10,
 492 celestite dissolution inferred by modelling results was not experimentally correlated with an increase
 493 of Sr concentration, which could be explained by strontianite precipitation (Garavaglia and
 494 Caramuscio, 1994). SEM observations on solid residue for MLS-A after basic leaching test at pH = 12.6
 495 (Figure 5) have shown a clearly altered celestite with a preferential dissolution at grains edges.
 496 Quantitative EPMA measurements inferred that in the attacked areas, grains were completely
 497 depleted in sulfates and Sr content was close to 60 %wt, which is the ratio expected in strontium
 498 carbonates. For CS, assuming the presence of celestite (not seen by XRD analysis for this sample)
 499 resulted in a two orders of magnitude overestimation of Sr concentration at pH0. The higher
 500 proportion of carbonates in CS compared to MLS-A and MLS-B could have resulted in the
 501 incorporation of Sr as a solid solution in carbonated minerals (Lerouge et al. 2010), which was in
 502 better agreement with experimental results (Figure 4c).

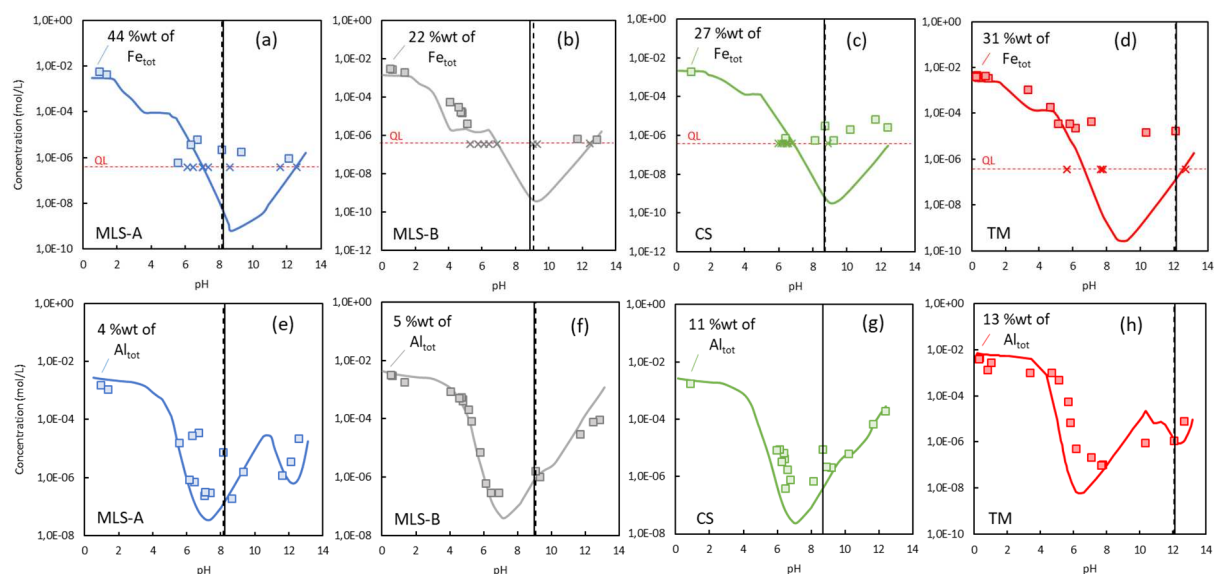


503

504 *Figure 5: SEM images of partially dissolved celestite following basic leaching test at pH = 12.6 in MLS-*
 505 *A. EPMA measurements are presented in weight percentage for two points: one at the grain core and*
 506 *one at the edge. Results inferred the disappearance of both sulfates and Mo at celestite edges while*
 507 *grains core still showed typical composition for Mo-bearing SrSO₄.*

508 Unlike strontium, sulfates (SO₄²⁻) concentrations can be impacted by the over- and undersaturation
 509 of several mineral phases so that it is often more difficult to discuss their evolutions. Celestite partial
 510 dissolution was shown to be responsible for at least a part of the rise in SO₄²⁻ concentrations at pH <
 511 7 in MLS-A (Figure 4e). At high pH values, SO₄²⁻ was a part of both contradictory mechanisms of
 512 celestite dissolution and ettringite precipitation so that its concentration did not depict strong
 513 variations. Modelling results for sulfates concentrations in TM (Figure 4h) were in agreement with
 514 experimental data at pH values below 10. For higher pH, and consistently with what was observed
 515 for Sr, concentrations were underestimated either because precipitation of ettringite was too high or
 516 because celestite dissolution was underestimated. For MLS-B (Figure 4f), SO₄²⁻ concentrations were
 517 reasonably well described by celestite partial dissolution at pH values above pH₀. However, the rise
 518 of SO₄²⁻ concentration at pH < 7 could not be explained by celestite dissolution alone and it has been
 519 assumed that a part of SO₄²⁻ was trapped in carbonated minerals and especially in calcite as
 520 previously suggested by studies focused on alkaline fly ash leachates (Schramke J.A., 1992). The same
 521 assumption was made in the case of CS. Finally, even though pyrite (FeS₂) dissolution in carbonated
 522 systems was already recorded in both acid and basic areas during pH dependence leaching tests
 523 (Drapeau, 2018), no direct insights of pyrite oxidation was observed in the present study. Only basic
 524 conditions might lead to a partial dissolution as inferred by modelling results. In agreement with the
 525 low amount of iron sulfides noticed in our samples (below the XRD detection limit and only few
 526 grains observed by SEM), pyrite was only introduced in our model at trace levels so that its
 527 contribution on SO₄ behavior would be negligible.

528 3.2.2.3. Iron and Aluminum



529 *Figure 6: Experimental and modelling results of Fe and Al concentrations as a function of pH during*
 530 *pH dependence leaching tests for MLS-A (a and e), MLS-B (b and f), CS (c and g) and TM (d and h).*
 531 *Marks and solid lines represent experimental and modelling data respectively while cross marks*
 532 *represent value below the QL. Vertical dashed and solid lines represent the experimental and*
 533 *modelled natural batch pH respectively.*

534 Fe behavior understanding is important since quantity of reactive surface sites for complexation
 535 phenomena would vary as iron oxides dissolve or precipitate. Experimental data have shown that Fe
 536 concentrations were often below or close to the QL of $0.2 \text{ mg}\cdot\text{kg}^{-1}$ (*i.e.* $4\cdot 10^{-7} \text{ mol}\cdot\text{L}^{-1}$) at $\text{pH} > 5$, which
 537 could be explained by the oversaturation of iron (hydr-)oxides such as goethite and/or ferrihydrite
 538 for such slightly acidic to strongly alkaline conditions. However, this trend was less clear in CS and TM
 539 (Figure 6c and d), where Fe concentrations in solution were regularly above QL resulting in their
 540 underestimation by the geochemical model. One has to keep in mind that eluates were only filtrated
 541 at $0.45 \mu\text{m}$, which limits but not prevents colloidal particles from being analyzed. Since our samples
 542 are almost completely depleted in OM, colloidal iron might rather occur as amorphous oxides either
 543 stable or being precursors for ferrihydrite precipitation (Van der Woude and De Bruyn, 1983). In all
 544 samples, at $\text{pH} < 5$, Fe concentrations increased sharply as dissolution of oxides became more and
 545 more important. For the most concentrated acid solution added in each sample, a maximum of Fe
 546 release was reached experimentally, which represented 25 wt%, 44 wt%, 21 wt% and 36 wt% of total
 547 Fe in CS, MLS-A, MLS-B and TM respectively. It pointed out the incomplete dissolution of both oxides
 548 and silicate minerals (Drapeau, 2018), which was well described by modelling results after
 549 modification of RSA for Fe-bearing phases. The best results were obtained by representing iron
 550 (hydr-)oxides with two different mineral forms: (i) goethite with a dissolution kinetically limited and

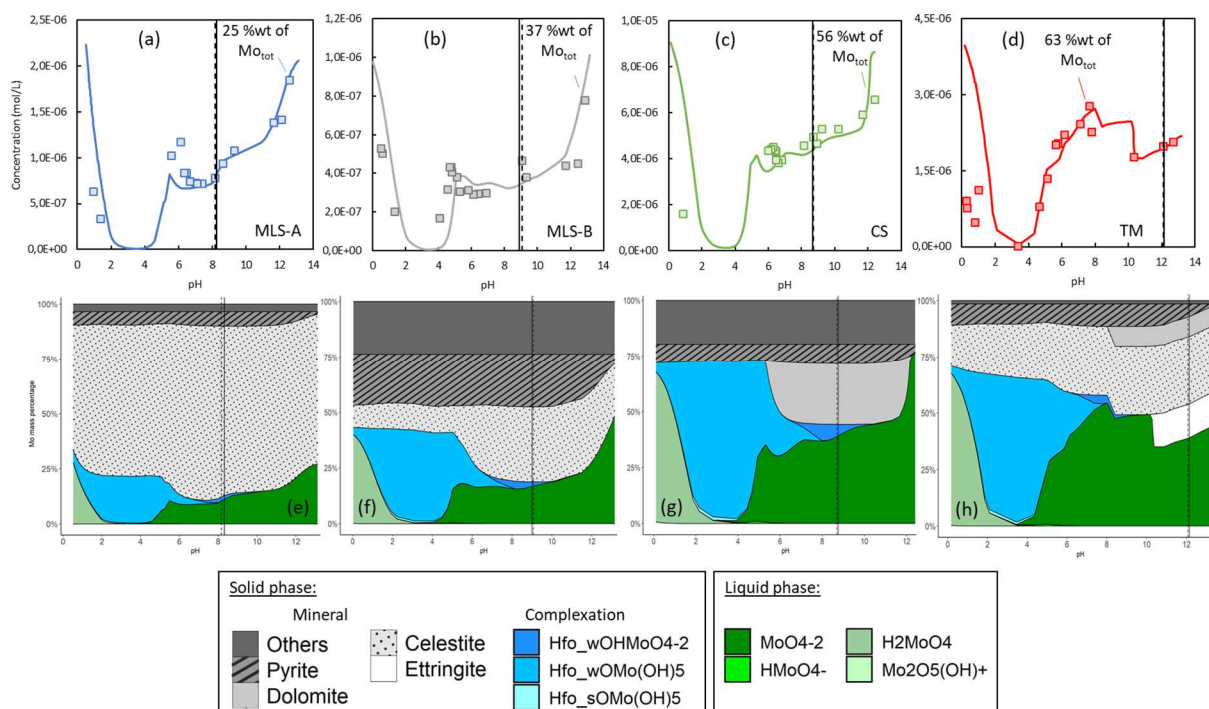
551 which was the seat of surface sites for complexation and (ii) amorphous ferrihydrite allowed to
 552 precipitate to control Fe leaching at pH > 5 but not considered for complexation reactions.

553 As Aluminum was concerned, at both ends of the pH range, incomplete dissolution of silicate phases
 554 (illite, albite, kaolinite...) initially present in the total assemblage resulted in a rise of Al concentration
 555 (Dijkstra et al. 2006). For pH values included between 5 and 10 approximately, this rise was
 556 mitigated by gibbsite precipitation. All four samples therefore presented a V-shaped curve for Al
 557 concentrations as a function of pH (see Figure 6e, 6f, 6g and 6h). Inflections in the V-shaped curves
 558 were observed in MLS-A and TM between pH = 10 and 12, consistently with ettringite precipitation
 559 as pH increased and ettringite dissolution as pH decreased for MLS-A and TM respectively.

560 3.2.3. Trace elements

561 Experimental and modelling results for Mo and Sb concentrations during pH dependence leaching
 562 tests are given for each sample in Figure 7 and Figure 8 respectively. Each pH dependency curve is
 563 presented along with a surface area plot representing repartition of Mo or Sb between solid and
 564 liquid phases over the whole pH range. These results are expressed in weight percentage calculated
 565 from modelling data and total TE content measured by TCA.

566 3.2.3.1. Molybdenum



567 *Figure 7: Experimental and modelling results of Mo concentrations as a function of pH during pH*
 568 *dependence leaching tests for MLS-A (a), MLS-B (b), CS (c) and TM (d). Marks and solid lines represent*

569 *experimental and modelling data respectively. Vertical dashed and solid lines represent the*
570 *experimental and modelled natural batch pH respectively. For each pH dependency curve, a*
571 *corresponding area plot representing Mo repartition between solid and liquid phase is given below.*
572 *Mass balance has been made regarding the total Mo concentrations measured by total content*
573 *analysis for each sample*

574 Assuming 0.08 mg of Mo per gram of celestite in MLS-A and MLS-B allowed us to describe well Mo
575 concentrations for pH > 5 (Figure 7a and b) directly confirming SEM/EPMA observations. For both
576 samples, two leaching maxima were noticed in relation to celestite partial dissolution at pH = 6.2
577 and 12.5 for MLS-A and at pH = 5.5 and 12.5 for MLS-B. SEM/EPMA quantitative measurement on
578 solid residue for MLS-A after basic neutralization capacity test (pH = 12.6) presented in Figure 5 have
579 shown the attacked edges of celestite grains completely depleted in Mo. On the contrary, celestite
580 core still presented a Mo content close to what was observed on the raw sample (*i.e.* 0.1 %wt). To
581 our knowledge, no direct associations have been referenced between Mo and evaporitic salts like
582 celestite (Smedley and Kinniburgh, 2017) even if evaporites have long been suspected to be a source
583 of TE and especially oxyanions (Kohut and Dudas, 1993). As far as excavated earths are concerned,
584 Tabelin et al. (2014) outlined significant associations between evaporitic salts (anhydrite, mirabilite,
585 nahcolite...) and oxyanionic species (As, B and Se). Mechanisms of incorporation of these elements in
586 trace amounts are related to ancient sedimentation in marine environment (Tabelin et al. 2018)
587 which could be consistent with the Parisian basin enrichment scenario. Ong et al. (1997) inferred that
588 in areas with high Mo contamination levels, the conditions recently created by saline agricultural
589 evaporation ponds rather led to the precipitation of CaMoO_4 than Mo incorporation in evaporites.
590 Hence, one can suggest that low Mo content (as occurring in our samples) could be of primary
591 importance for the emergence of such associations.

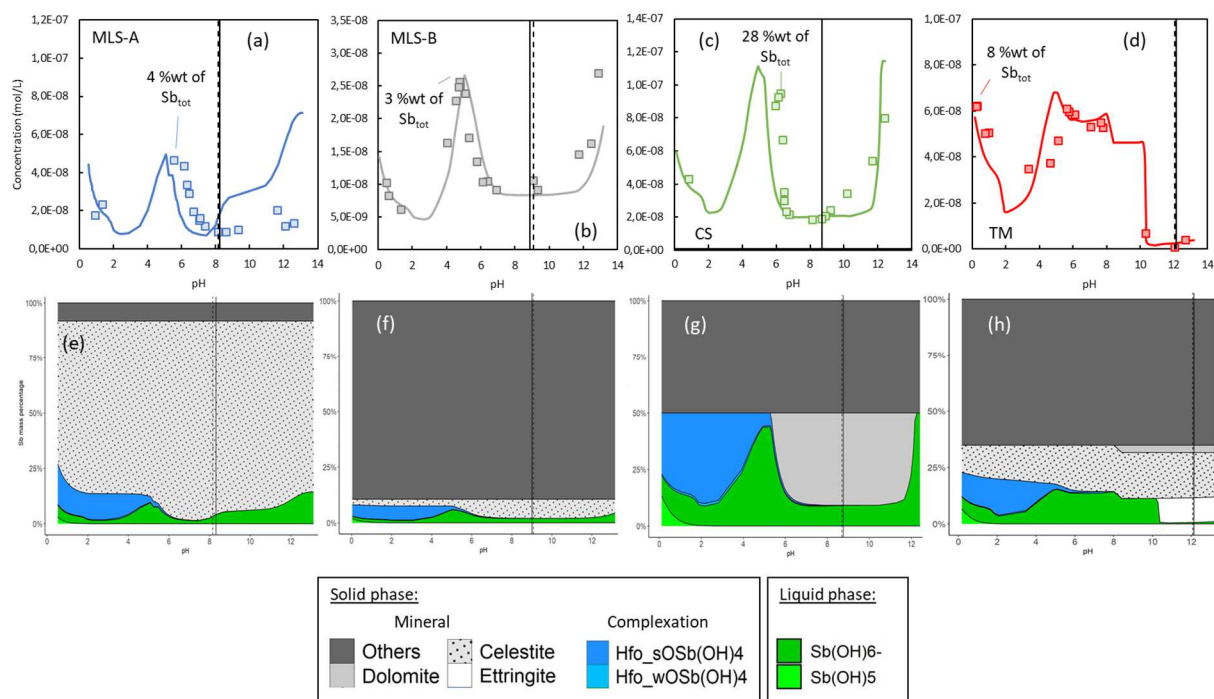
592 Mo behavior at pH < 6 was similar in all samples. A drop of Mo concentrations was observed as
593 complexation at oxides surfaces became more and more important until Mo was almost totally in
594 solid form between pH = 2 and 4. The simultaneous kinetically limited dissolution of Mo-bearing
595 phases and goethite at pH < 2 led to a final rise of Mo concentrations, mostly released in a doubly
596 protonated form (H_2MoO_4). Other similarities could be seen in pyrite behavior for all samples, which
597 systematically showed a partial dissolution at pH > 11 accounting for a relatively small fraction of
598 total Mo release.

599 For CS (Figure 7c), Mo behavior revealed a strong pH dependency, showing leaching minimum and
600 maximum at pH = 1 and 12.5 respectively. The first acid addition resulted in a small decrease of Mo
601 concentration, as complexation at oxides surface sites was slowly favored. The subsequent
602 dissolution of dolomite (modelled at pH = 6 and observed at pH = 6.8) triggered an increase of Mo
603 concentration quickly compensated by the growing importance of complexation. In the basic area,

604 first NaOH addition led to a slight Mo concentration increase due to Mo desorption as oxides surface
605 charges became more and more negative. The final Mo increase (pH > 10) was exaggerated by
606 modelling results probably because of an overestimation of brucite precipitation (triggering dolomite
607 dissolution and therefore Mo release). Our model failed to improve further Mo concentration
608 description even considering time and pH dependencies for brucite precipitation (Dijkstra et al. 2006;
609 Pokrovsky and Schott, 2004).

610 Consistently with the mix of CS and MLS-A geological formation represented in TM, both celestite
611 and dolomite were considered to bear substantial quantities of Mo. Furthermore, lime addition
612 disfavored complexation phenomena and created conditions (pH > 10) for celestite partial
613 dissolution enhancing Mo mobility. Part of this labile Mo was removed during slurry treatment
614 process resulting in the Mo impoverishment outlined in section 3.1.1. Nevertheless, non-negligible
615 amounts of Mo could also have been incorporated in ettringite (Cornelis et al., 2008). Although not
616 particularly favored by Mo large size (Zhang and Reardon, 2003), SO_4^{2-} replacement by Mo during
617 ettringite precipitation might explain the Mo concentrations increase between pH = 10 and 7 (Figure
618 7d). For such pH values, both celestite and dolomite were oversaturated so that no particular impact
619 on Mo concentrations were expected. On the other hand, ettringite was shown to dissolve quickly at
620 pH < 10, which allowed us to describe Mo behavior assuming 0.008 mg of Mo per gram of ettringite.
621 At pH values below 7, Mo release triggered by successive celestite and carbonates dissolutions were
622 hidden by complexation at oxides surfaces.

623 3.2.3.2. Antimony



624 *Figure 8: Experimental and modelling results of Sb concentrations as a function of pH during pH*
 625 *dependence leaching tests for MLS-A (a), MLS-B (b), CS (c) and TM (d). Marks and solid lines represent*
 626 *experimental and modelling data respectively. Vertical dashed and solid lines represent the*
 627 *experimental and modelled natural batch pH respectively. For each pH dependency curve, a*
 628 *corresponding area plot representing Sb repartition between solid and liquid phase is given below.*
 629 *Mass balance has been made regarding the total Sb concentrations as measured by total content*
 630 *analysis for each sample*

631 For each sample, Sb concentrations presented similar features compared to Mo over the whole pH
 632 range (Figure 8). Repartition of Sb was not investigated by SEM/EPMA analysis because of DL issues,
 633 but modelling results strongly suggested that celestite associations were also the main factor
 634 affecting its mobility during pH dependence leaching tests in MLS-A and MLS-B. This was particularly
 635 clear for MLS-B (Figure 8b), where assuming 0.005 mg of Sb per gram of celestite was sufficient to
 636 describe Sb concentrations evolutions at pH > 4.5. At the end and after the carbonates buffer area
 637 (pH = 4.5 and below), Sb concentrations drop off in all samples because of the growing importance of
 638 complexation at these favoring pH conditions. Assumptions made regarding Sb complexation
 639 occurring through simple ligand exchange between reactive surface sites and Sb(OH)_6^- (Cornelis et al.
 640 2012) satisfyingly described experimental observations. Sb seemed to be proportionally more
 641 retained than Mo at low pH. This might be due to its aqueous speciation in those pH and redox
 642 conditions, where a part of Sb was still under the Sb(OH)_6^- form directly concerned by complexation
 643 while the only Mo aqueous form at pH < 2 (H_2MO_4) was not expected to be involved in complexation.
 644 One can note that surface plot presented for MLS-B and TM (Figure 8f and h) might largely

645 overestimate the non-leachable Sb proportion since it was computed by fixing a Sb total content
646 equals to QL. Despite the slightly higher proportion of 0.007 mg of Sb per grams of celestite, the main
647 difference between Sb behavior in MLS-A and MLS-B was seen at pH above pH_0 . Indeed, for MLS-A,
648 the leaching maximum corresponding to celestite acidic partial dissolution ($pH = 6.2$) was not
649 symmetrically retrieved at $pH > 12$, where Sb concentrations remained relatively low ($< 1.9 \cdot 10^{-8}$
650 $\text{mol} \cdot \text{L}^{-1}$). Sb concentrations were systematically under-saturated regarding calcium antimonate
651 because of the low Sb total content. We suggest that Sb was incorporated in ettringite structure
652 during pH dependence leaching tests at $pH > 10$ by replacement of SO_4^{2-} (Cornelis et al. 2008).
653 Indeed, on one hand, ettringite was clearly shown to precipitate in MLS-A (see section 3.2.2.1) and,
654 on the other hand, this behavior was not acknowledged in MLS-B or CS where no ettringite was
655 formed. Figure 8e could be used to point out the importance of celestite on Sb overall speciation in
656 MLS-A. Moreover, at pH_0 , Sb seemed to be mainly associated with unreactive mineral, consistently
657 with its relatively low mobility compared to Mo.

658 Sb concentrations in CS (Figure 8c) during pH dependence leaching tests could be described by
659 assuming a speciation close to what was stated for Mo. Indeed, considering a proportion of 0.002 mg
660 of Sb per grams of dolomite, we managed to represent both acid and basic maximum leached
661 concentrations, which were highly impacted by dolomite dissolution.

662 Finally, results for TM could be used to outline the main factor affecting Sb behavior (Figure 8d).
663 Precipitated ettringite was suggested to control Sb release between $pH = 7$ and 13. The lowest Sb
664 concentration in solution was seen at pH_0 because of ettringite initial presence and subsequent
665 precipitation during experiment, which was likely to have a stabilizing effect. Representation of Sb
666 complexation at oxides surfaces in TM was not as satisfactory as for other samples. Indeed
667 complexation was first overestimated between $pH = 6$ and $pH = 8$ resulting in a drop of Sb
668 concentrations inconsistent with experimental results. A second shift between modelling and
669 experimental results occurred at acidic pH resulting in considering a too high proportion of Sb in the
670 solid phase. Although some discrepancies persisted between modelling and experimental results in
671 TM, it is interesting to point out that hypothesis made to describe CS and MLS-A major and trace
672 elements speciation were also applicable to define this more complex material having undergone
673 particular pretreatments (liming, filtration...). These conclusions might shed light to the fact that,
674 upon contact with air in a storage scenario, Sb and in a lesser extent Mo mobility in tunnel mucks
675 might be increased. Indeed, pH is expected to decrease following carbonation until an endpoint of 8
676 is reached (Dijkstra et al., 2019), which will trigger the release of TE incorporated in ettringite. Such
677 conclusions consolidate the usefulness of geochemical modelling to help overcome issues in the
678 management of excavated materials untreated or with particular treatments.

679 **4. CONCLUSION**

680 Excavated earths from Grand Paris Express construction sites often present high mobility regarding
681 particular trace elements. This study was aiming to present a complete overview of Mo and Sb
682 speciation in four different excavated rocks and soils through direct and indirect analysis coupled
683 with geochemical modelling. Among the four samples, three were raw materials only representing
684 one geological formation, while the fourth was a mix of two geological formations, which had been
685 treated (liming, filtration...) in a slurry treatment plan before sampling for the present study. All
686 samples were mainly carbonated and TE natural contamination only occurred through low levels.
687 Total mineral assemblages were modelled assuming kinetically dependent dissolution for each
688 mineral phases (excepted carbonates and gypsum). This approach could be determining to help us
689 understand the global behavior of excavated earths and soils in different scenarii (e.g. reuse,
690 storage...). Mo was seen in association with pyrite in all samples probably incorporated as a solid
691 solution. The Mo associated with pyrite was suggested to be released only under basic conditions.
692 Complexation at iron (hydr-)oxides surfaces was seen to control Mo and Sb at acidic pH and was
693 satisfyingly described by the Generalized Two Layer Model. Mo and Sb associations with celestite
694 were clearly identified in both marly limestones so that, in celestite-rich samples, celestite
695 dissolution should be monitored to predict Mo and Sb long-term mobility. In the calcareous sample,
696 an ambiguous behavior of Mo and Sb was noticed, where incorporation into carbonates was
697 preferred to describe their speciation compared to celestite associations. Although only assumed
698 from indirect characterization methods, it could partly explain the highest mobility attested in this
699 sample were Mo exchangeable fraction would therefore be impacted by a large proportion of Mo
700 associated with carbonates. Finally, hypothesis made for modelling both calcareous and marly
701 limestone samples were extended to describe satisfyingly Mo and Sb behavior in the tunnel boring
702 mucks, in which incorporation of both oxyanions during ettringite precipitation has mitigated their
703 leaching at the natural pH of the mucks. In terms of environmental management of the excavated
704 materials, the results presented here emphasize the importance of pH on TE leaching behavior
705 especially for alkaline tunnel mucks, which would undergo a pH decrease upon contact with the air in
706 a context of storage.

707

708 **ACKNOWLEDGMENTS**

709 The authors would like to thank N. Marty (BRGM, France) for its help in implementing kinetic
710 considerations in all geochemical models as long as for his valuable comments on model structures
711 and reliability. SEM/EPMA analysis were realized with the great help of C. Duee and G. Wille while N.
712 Maubec performed XRD analysis. Special thanks also go to T. Conte and the BRGM laboratory team,
713 which performed all liquid analysis following pH dependence leaching tests, standardized leaching
714 tests and TCA. Finally, this study was financially supported by Bouygues Travaux Publics (France) as a
715 part of IMMOTERRE research and development project.

716

717 **REFERENCES**

- 718 ADEME, 2017. Déchets chiffres-clés, ADEME Editions.
- 719 AFNOR, 2016. NF EN ISO 17294-2 - Water quality — Application of inductively coupled plasma mass
720 spectrometry (ICP-MS) — Part 2: Determination of selected elements including uranium isotopes
- 721 AFNOR, 2015. NF EN 14429 : Characterization of waste — Leaching behaviour test — Influence of pH
722 on leaching with initial acid/base addition
- 723 AFNOR, 2009. NF EN ISO 11885 - Determination of selected elements by inductively coupled plasma
724 optical emission spectrometry (ICP-OES)
- 725 AFNOR, 2002. NF EN 12457-2 - Characterization of waste - Leaching - Compliance test for leaching of
726 granular waste materials and sludges - Part 2 : one stage batch test at a liquid to solid ratio of 10 l/kg
727 for materials with particle size below 4 mm (without or with size reduction)
- 728 AFNOR, 1995. NF ISO 10694 : Dosage du carbone organique et du carbone total après combustion
729 sèche (analyse élémentaire)
- 730 Albinati, A., Willis, B.T.M., 2006. The Rietveld method, in: International Tables for Crystallography.
731 American Cancer Society, pp. 710–712. <https://doi.org/10.1107/97809553602060000614>
- 732 Arai, Y., 2010. Arsenic and Antimony, in: Trace Elements in Soils. John Wiley & Sons, Ltd, pp. 381–
733 407. <https://doi.org/10.1002/9781444319477.ch16>
- 734 Auroy, M., Poyet, S., Le Bescop, P., Torrenti, J.-M., Charpentier, T., Moskura, M., Bourbon, X., 2018.
735 Comparison between natural and accelerated carbonation (3% CO₂): Impact on mineralogy,
736 microstructure, water retention and cracking. Cement and Concrete Research 109, 64–80.
737 <https://doi.org/10.1016/j.cemconres.2018.04.012>
- 738 Blanc, Ph., Lassin, A., Piantone, P., Azaroual, M., Jacquemet, N., Fabbri, A., Gaucher, E.C., 2012.
739 Thermoddem: A geochemical database focused on low temperature water/rock interactions and
740 waste materials. Applied Geochemistry 27, 2107–2116.
741 <https://doi.org/10.1016/j.apgeochem.2012.06.002>
- 742 Boynton, R.S., 1966. Chemistry and Technology of Lime and Limestone 520–520.
- 743 BRGM, 2020. Guide de valorisation hors site des terres excavées non issues de sites et sols pollués
744 dans des projets d'aménagement.

745 Buttress, A.J., Grenfell, J.R.A., Airey, G.D., 2013. The role of ettringite in the deterioration of artificial
746 lime stabilised soils: a microstructural study. *Road Materials and Pavement Design* 14, 586–614.
747 <https://doi.org/10.1080/14680629.2013.779306>

748 Cabrerizo, A., Bulteel, D., Waligora, J., Landrot, G., Fonda, E., Olard, F., 2020. Chemical, mineralogical,
749 and environmental characterization of tunnel boring muds for their valorization in road construction:
750 a focus on molybdenum characterization. *Environ Sci Pollut Res.* [https://doi.org/10.1007/s11356-](https://doi.org/10.1007/s11356-020-09969-6)
751 [020-09969-6](https://doi.org/10.1007/s11356-020-09969-6)

752 Cornelis, G., Gerven, T.V., Vandecasteele, C., 2012. Antimony leaching from MSWI bottom ash:
753 Modelling of the effect of pH and carbonation. *Waste Management* 32, 278–286.
754 <https://doi.org/10.1016/j.wasman.2011.09.018>

755 Cornelis, G., Johnson, C.A., Gerven, T.V., Vandecasteele, C., 2008. Leaching mechanisms of oxyanionic
756 metalloid and metal species in alkaline solid wastes: A review. *Applied Geochemistry* 23, 955–976.
757 <https://doi.org/10.1016/j.apgeochem.2008.02.001>

758 Coussy, S., Benzaazoua, M., Blanc, D., Moszkowicz, P., Bussière, B., 2011. Arsenic stability in
759 arsenopyrite-rich cemented paste backfills: A leaching test-based assessment. *Journal of Hazardous*
760 *Materials* 185, 1467–1476. <https://doi.org/10.1016/j.jhazmat.2010.10.070>

761 Dijkstra, J.J., Comans, R.N.J., Schokker, J., Meulen, M.J. Van Der, 2019. The geological significance of
762 novel anthropogenic materials: Deposits of industrial waste and by-products. *Anthropocene* 28,
763 100229. <https://doi.org/10.1016/j.ancene.2019.100229>

764 Dijkstra, J.J., Meeussen, J.C.L., Comans, R.N.J., 2009. Evaluation of a Generic Multisurface Sorption
765 Model for Inorganic Soil Contaminants. *Environ. Sci. Technol.* 43, 6196–6201.
766 <https://doi.org/10.1021/es900555g>

767 Dijkstra, J.J., van der Sloot, H.A., Comans, R.N.J., 2006. The leaching of major and trace elements
768 from MSWI bottom ash as a function of pH and time. *Applied Geochemistry* 21, 335–351.
769 <https://doi.org/10.1016/j.apgeochem.2005.11.003>

770 Dou, W., Zhou, Z., Jiang, L.-M., Jiang, A., Huang, R., Tian, X., Zhang, W., Chen, D., 2017. Sulfate
771 removal from wastewater using ettringite precipitation: Magnesium ion inhibition and process
772 optimization. *Journal of Environmental Management* 196, 518–526.
773 <https://doi.org/10.1016/j.jenvman.2017.03.054>

774 Drapeau, C., 2018. Mesure et modélisation de la mobilité et de la spéciation des éléments majeurs et
775 traces métalliques au sein de matrices complexes polluées en fonction du pH : application aux
776 sédiments urbains et déchets miniers (phdthesis). Université de Lyon.

777 Dzombak, D.A., Morel, F.M.M., 1990. Surface Complexation Modeling: Hydrous Ferric Oxide. John
778 Wiley & Sons.

779 Garavaglia, R., Caramuscio, P., 1994. Coal Fly-Ash Leaching Behaviour and Solubility Controlling
780 Solids, in: Goumans, J.J.J.M., van der Sloot, H.A., Aalbers, Th.G. (Eds.), Studies in Environmental
781 Science, Environmental Aspects of Construction with Waste Materials. Elsevier, pp. 87–102.
782 [https://doi.org/10.1016/S0166-1116\(08\)71450-X](https://doi.org/10.1016/S0166-1116(08)71450-X)

783 Giffaut, E., Grivé, M., Blanc, Ph., Vieillard, Ph., Colàs, E., Gailhanou, H., Gaboreau, S., Marty, N., Madé,
784 B., Duro, L., 2014. Andra thermodynamic database for performance assessment: ThermoChimie.
785 Applied Geochemistry, Geochemistry for Risk Assessment: Hazardous waste in the Geosphere 49,
786 225–236. <https://doi.org/10.1016/j.apgeochem.2014.05.007>

787 Gis Sol, 2011. L'état des sols de France. Groupement d'intérêt scientifique sur les sols, 188p.

788 Gourcy, L., Winckel, A., Brugeron, A., 2011. RP-57344-FR - Origine du sélénium et compréhension des
789 processus dans les eaux du bassin Seine-Normandie.

790 Grenthe, I., Puigdomènech, I., Agency, O.N.E., 1997. Modelling in Aquatic Chemistry. Nuclear Energy
791 Agency, Organisation for Economic Co-operation and Development.

792 Gustafsson, J.P., 2003. Modelling molybdate and tungstate adsorption to ferrihydrite. Chemical
793 Geology 200, 105–115. [https://doi.org/10.1016/S0009-2541\(03\)00161-X](https://doi.org/10.1016/S0009-2541(03)00161-X)

794 Halmi, M.I.E., Ahmad, S.A., 2014. Chemistry, biochemistry, toxicity and pollution of molybdenum: A
795 mini review. Journal of Biochemistry, Microbiology and Biotechnology 2, 1–6.

796 Hans Wedepohl, K., 1995. The composition of the continental crust. Geochimica et Cosmochimica
797 Acta 59, 1217–1232. [https://doi.org/10.1016/0016-7037\(95\)00038-2](https://doi.org/10.1016/0016-7037(95)00038-2)

798 Harkness, J.S., Darrah, T.H., Moore, M.T., Whyte, C.J., Mathewson, P.D., Cook, T., Vengosh, A., 2017.
799 Naturally Occurring versus Anthropogenic Sources of Elevated Molybdenum in Groundwater:
800 Evidence for Geogenic Contamination from Southeast Wisconsin, United States [WWW Document].
801 <https://doi.org/10.1021/acs.est.7b03716>

802 He, M., Wang, X., Wu, F., Fu, Z., 2012. Antimony pollution in China. Science of the Total Environment
803 421–422, 41–50. <https://doi.org/10.1016/j.scitotenv.2011.06.009>

804 Herath, I., Vithanage, M., Bundschuh, J., 2017. Antimony as a global dilemma: Geochemistry,
805 mobility, fate and transport. *Environmental Pollution* 223, 545–559.
806 <https://doi.org/10.1016/j.envpol.2017.01.057>

807 Kohut, C.K., Dudas, M.J., 1993. Evaporite mineralogy and trace-element content of salt-affected soils
808 in Alberta. *Can. J. Soil. Sci.* 73, 399–409. <https://doi.org/10.4141/cjss93-042>

809 Lerouge, C., Gaucher, E.C., Tournassat, C., Negrel, P., Crouzet, C., Guerrot, C., Gautier, A., Michel, P.,
810 Vinsot, A., Buschaert, S., 2010. Strontium distribution and origins in a natural clayey formation
811 (Callovian-Oxfordian, Paris Basin, France): A new sequential extraction procedure. *Geochimica et*
812 *Cosmochimica Acta* 74, 2926–2942. <https://doi.org/10.1016/j.gca.2010.02.013>

813 Leuz, A.-K., Mönch, H., Johnson, C.A., 2006. Sorption of Sb(III) and Sb(V) to Goethite: Influence on
814 Sb(III) Oxidation and Mobilization. *Environ. Sci. Technol.* 40, 7277–7282.
815 <https://doi.org/10.1021/es061284b>

816 Marty, N.C.M., Claret, F., Lassin, A., Tremosa, J., Blanc, P., Madé, B., Giffaut, E., Cochepin, B.,
817 Tournassat, C., 2015. A database of dissolution and precipitation rates for clay-rocks minerals.
818 *Applied Geochemistry, Geochemical Speciation Codes and Databases* 55, 108–118.
819 <https://doi.org/10.1016/j.apgeochem.2014.10.012>

820 Meima, J.A., Comans, R.N.J., 1998. Reducing Sb-leaching from municipal solid waste incinerator
821 bottom ash by addition of sorbent minerals. *Journal of Geochemical Exploration* 62, 299–304.
822 [https://doi.org/10.1016/S0375-6742\(97\)00044-7](https://doi.org/10.1016/S0375-6742(97)00044-7)

823 Merlet, C., 1994. An accurate computer correction program for quantitative electron probe
824 microanalysis. *Mikrochim Acta* 114, 363–376. <https://doi.org/10.1007/BF01244563>

825 Merlet, C., 1992. Quantitative Electron Probe Microanalysis: New Accurate $\Phi(\rho z)$ Description, in:
826 Boekestein, A., Pavićević, M.K. (Eds.), *Electron Microbeam Analysis, Mikrochimica Acta*. Springer,
827 Vienna, pp. 107–115. https://doi.org/10.1007/978-3-7091-6679-6_8

828 Milne, C.J., Kinniburgh, D.G., van Riemsdijk, W.H., Tipping, E., 2003. Generic NICA–Donnan Model
829 Parameters for Metal-Ion Binding by Humic Substances. *Environ. Sci. Technol.* 37, 958–971.
830 <https://doi.org/10.1021/es0258879>

831 Müller, B., Granina, L., Schaller, T., Ulrich, A., Wehrli, B., 2002. P, As, Sb, Mo, and Other Elements in
832 Sedimentary Fe/Mn Layers of Lake Baikal. *Environ. Sci. Technol.* 36, 411–420.
833 <https://doi.org/10.1021/es010940z>

834 OJEC, 2003. Council Decision of 19 December 2002 establishing criteria and procedures for the
835 acceptance of waste at landfills pursuant to Article 16 of and Annex II to Directive 1999/31/EC.
836 Official Journal of the European Communities, January 16, 2003.

837 OJEC, 1999. Council Directive 1999/31/EC of 26 April 1999 on the landfill of waste. Official Journal of
838 the European Communities, July 16, 1999.

839 OJEU, 2008. Directive 2008/98/EC of the European Parliament and of the Council of 19 November
840 2008 on waste and repealing certain Directives. Official Journal of the European Union, November
841 22, 2008.

842 Ong, C.G., Herbel, M.J., Dahlgren, R.A., Tanji, K.K., 1997. Trace Element (Se, As, Mo, B) Contamination
843 of Evaporites in Hypersaline Agricultural Evaporation Ponds. *Environ. Sci. Technol.* 31, 831–836.
844 <https://doi.org/10.1021/es960531g>

845 Parkhurst, D.L., Appelo, C.A.J., 2013. Description of input and examples for PHREEQC version 3: a
846 computer program for speciation, batch-reaction, one-dimensional transport, and inverse
847 geochemical calculations, *Techniques and Methods*. U.S. Geological Survey, Reston, VA.
848 <https://doi.org/10.3133/tm6A43>

849 Pokrovsky, O.S., Schott, J., 2004. Experimental study of brucite dissolution and precipitation in
850 aqueous solutions: surface speciation and chemical affinity control. *Geochimica et Cosmochimica*
851 *Acta* 68, 31–45. [https://doi.org/10.1016/S0016-7037\(03\)00238-2](https://doi.org/10.1016/S0016-7037(03)00238-2)

852 Rietveld, H.M., 1969. A profile refinement method for nuclear and magnetic structures. *J Appl Cryst*
853 2, 65–71. <https://doi.org/10.1107/S0021889869006558>

854 Roper, A.J., Williams, P.A., Filella, M., 2012. Secondary antimony minerals: Phases that control the
855 dispersion of antimony in the supergene zone. *Geochemistry, Antimony* 72, 9–14.
856 <https://doi.org/10.1016/j.chemer.2012.01.005>

857 Schramke, J.A., 1992. Neutralization of alkaline coal fly ash leachates by CO₂(g). *Applied*
858 *Geochemistry, Minerals for Future Materials* 7, 481–492. [https://doi.org/10.1016/0883-2927\(92\)90008-Q](https://doi.org/10.1016/0883-2927(92)90008-Q)

860 SGP, 2019. « Le défi de la valorisation des déblais ». The challenge of managing the excavated soils.
861 Société du Grand Paris, April 5th 2019. Retrieved from:
862 <https://www.societedugrandparis.fr/info/gestion-et-valorisation-des-d%C3%A9blais>

863 Singer, A., 1977. Dissolution of Two Australian Palygorskites in Dilute Acid. *Clays Clay Miner.* 25, 126–
864 130. <https://doi.org/10.1346/CCMN.1977.0250209>

865 Smedley, P.L., Cooper, D.M., Lapworth, D.J., 2014. Molybdenum distributions and variability in
866 drinking water from England and Wales. *Environ Monit Assess* 186, 6403–6416.
867 <https://doi.org/10.1007/s10661-014-3863-x>

868 Smedley, P.L., Edmunds, W.M., 2002. Redox Patterns and Trace-Element Behavior in the East
869 Midlands Triassic Sandstone Aquifer, U.K. *Groundwater* 40, 44–58. [https://doi.org/10.1111/j.1745-
870 6584.2002.tb02490.x](https://doi.org/10.1111/j.1745-6584.2002.tb02490.x)

871 Smedley, P.L., Kinniburgh, D.G., 2017. Molybdenum in natural waters: A review of occurrence,
872 distributions and controls. *Applied Geochemistry* 84, 387–432.
873 <https://doi.org/10.1016/j.apgeochem.2017.05.008>

874 Sterckeman, T., Douay, F., Baize, D., Fourrier, H., Proix, N., Schwartz, C., 2006. Trace elements in soils
875 developed in sedimentary materials from Northern France. *Geoderma* 136, 912–929.
876 <https://doi.org/10.1016/j.geoderma.2006.06.010>

877 Tabelin, C.B., Hashimoto, A., Igarashi, T., Yoneda, T., 2014. Leaching of boron, arsenic and selenium
878 from sedimentary rocks: I. Effects of contact time, mixing speed and liquid-to-solid ratio. *Science of
879 The Total Environment* 472, 620–629. <https://doi.org/10.1016/j.scitotenv.2013.11.006>

880 Tabelin, C.B., Igarashi, T., Villacorte-Tabelin, M., Park, I., Opiso, E.M., Ito, M., Hiroyoshi, N., 2018.
881 Arsenic, selenium, boron, lead, cadmium, copper, and zinc in naturally contaminated rocks: A review
882 of their sources, modes of enrichment, mechanisms of release, and mitigation strategies. *Science of
883 The Total Environment* 645, 1522–1553. <https://doi.org/10.1016/j.scitotenv.2018.07.103>

884 Thanabalasingam, P., Pickering, W.F., 1990. Specific sorption of antimony (III) by the hydrous oxides
885 of Mn, Fe, and Al. *Water Air Soil Pollut* 49, 175–185. <https://doi.org/10.1007/BF00279519>

886 Trémosa, J., Castillo, C., Vong, C.Q., Kervévan, C., Lassin, A., Audigane, P., 2014. Long-term
887 assessment of geochemical reactivity of CO₂ storage in highly saline aquifers: Application to Ketzin,
888 In Salah and Snøhvit storage sites. *International Journal of Greenhouse Gas Control* 20, 2–26.
889 <https://doi.org/10.1016/j.ijggc.2013.10.022>

890 Tribouvillard, N., Riboulleau, A., Lyons, T., Baudin, F., 2004. Enhanced trapping of molybdenum by
891 sulfurized marine organic matter of marine origin in Mesozoic limestones and shales. *Chemical
892 Geology* 213, 385–401. <https://doi.org/10.1016/j.chemgeo.2004.08.011>

893 Van Der Woude, J.H.A., De Bruyn, P.L., 1983. Formation of colloidal dispersions from supersaturated
894 iron(III) nitrate solutions. I. Precipitation of amorphous iron hydroxide. *Colloids and Surfaces* 8, 55–
895 78. [https://doi.org/10.1016/0166-6622\(83\)80072-9](https://doi.org/10.1016/0166-6622(83)80072-9)

896 van Geen, A., Robertson, A.P., Leckie, J.O., 1994. Complexation of carbonate species at the goethite
897 surface: Implications for adsorption of metal ions in natural waters. *Geochimica et Cosmochimica*
898 *Acta* 58, 2073–2086. [https://doi.org/10.1016/0016-7037\(94\)90286-0](https://doi.org/10.1016/0016-7037(94)90286-0)

899 Vorlicek, T.P., Kahn, M.D., Kasuya, Y., Helz, G.R., 2004. Capture of molybdenum in pyrite-forming
900 sediments: role of ligand-induced reduction by polysulfides 1 1Associate editor: M. Goldhaber.
901 *Geochimica et Cosmochimica Acta* 68, 547–556. [https://doi.org/10.1016/S0016-7037\(03\)00444-7](https://doi.org/10.1016/S0016-7037(03)00444-7)

902 Wilson, S.C., Lockwood, P.V., Ashley, P.M., Tighe, M., 2010. The chemistry and behaviour of antimony
903 in the soil environment with comparisons to arsenic: A critical review. *Environmental Pollution* 158,
904 1169–1181. <https://doi.org/10.1016/j.envpol.2009.10.045>

905 Young, R.A. (Ed.), 1995. *The Rietveld Method*, International Union of Crystallography Monographs on
906 Crystallography. Oxford University Press, Oxford, New York. Zhang, M., Reardon, E.J., 2003. Removal
907 of B, Cr, Mo, and Se from Wastewater by Incorporation into Hydrocalumite and Ettringite. *Environ.*
908 *Sci. Technol.* 37, 2947–2952. <https://doi.org/10.1021/es020969i>

909